Study of magnetic skyrmions in square lattice antiferromagnets

David Leonardo Ramos Salamanca

Trabajo de Grado para optar al título de Magíster en Física

Director

Pierre Pujol

Doctor en Ciencias

Co-Director

Luis A. Núñez

Doctor en Ciencias

Universidad Industrial de Santander

Facultad de Ciencias

Escuela de Física

Bucaramanga

2023

Contents

List of Figures

Resumen

Título: Estudio de skyrmiones magnéticos en materiales antiferromagnéticos de red cuadrada. [*]

Autores: David Leonardo Ramos Salamanca [**]

Palabras Clave: Skyrmiones magnéticos, Skyrmiones antiferromagnéticos, Simulaciones de Monte Carlo

Descripción: Los skyrmiones magnéticos son texturas de espín similares a partículas que se forman en materiales magnéticos quirales. La topología no trivial de los skyrmiones les otorga una gran estabilidad y los convierte en candidatos prometedores para ser la base de nuevos dispositivos lógicos y de almacenamiento de información. Los skyrmiones magnéticos se han observado en muchos materiales ferromagnéticos y se ha predicho que existen en materiales antiferromagnéticos, pero aún no se han observado. Recientemente, ha habido un gran interés en los skyrmions antiferromagnéticos, ya que se han encontrado más adecuados para aplicaciones de almacenamiento de datos. Esto ha resultado en un esfuerzo por determinar las condiciones bajo las cuales se pueden formar skyrmiones antiferromagnéticos.

En esta tesis, nos centramos primero en el estudio analítico del tamaño de skyrmiones ferromagnéticos aislados basados en un modelo continuo. Reproducimos el trabajo seminal de Belavin y Polyakov sobre skyrmions ferromagnéticos y mostramos cómo, para un conjunto particular de modelos solubles, las interacciones comunes presentes en los materiales ferromagnéticos quirales establecen una escala de tamaño óptima para los skyrmions de Belavin-Polyakov, que de otro modo no tendrían escala. Luego estudiamos numéricamente la escala de tamaño de skyrmions aislados que difieren ligeramente de los modelos analíticamente solubles para el ferromagnético de plano fácil $Fe_{0.7}Co_{0.3}Si$. Por último, presentamos un nuevo ansatz para perfiles demagnetización de skyrmiones aislados que reproduce el comportamiento de las soluciones numéricas.

Posteriormente, centramos nuestra atención en los materiales antiferromagnéticos. Estudiamos numéricamente skyrmiones aislados en materiales antiferromagnéticos quirales con anisotropía de eje fácil en presencia de un campo magnético. Encontramos que hay una región del espacio de fase donde las soluciones aisladas de skyrmion tienen un tamaño finito y una energía más baja que la fase antiferromagnética. Además, observamos que los campos magnéticos aumentan la estabilidad de los skyrmiones antiferromagnéticos aislados. Además, utilizando simulaciones de Monte Carlo, confirmamos que existe una región del espacio de fase donde los skyrmiones antiferromagnéticos son configuraciones estables a temperaturas finitas incluso en ausencia de un campo magnético. Finalmente, observamos que los campos magnéticos aumentan el tamaño de los skyrmions antiferromagnéticos.

---

[*] Trabajo de investigación

[**] Facultad Ciencias. Escuela de Física.

Abstract

Title: Study of magnetic skyrmions in square lattice antiferromagnets. *

Author: David Leonardo Ramos Salamanca **

Keywords: Magnetic skyrmions, Antiferromagnetic skyrmions, Monte Carlo simulations

Descripton: Magnetic skyrmions are particle-like spin textures that form in chiral magnets. The non-trivial topology of skyrmions grants them great stability and makes them promising candidates to be the base of new information storage and logic devices. Magnetic skyrmions have been observed in many ferromagnetic materials and they have been predicted to exist in antiferromagnets but they have not been observed yet. Recently, there has been great interest in antiferromagnetic skyrmions as they have been found more suitable for applications in data storage. This has resulted in an effort to determine the conditions under which antiferromagnetic skyrmions can form.

In this thesis, we first focus on the analytical study of the size of isolated ferromagnetic skyrmions based on a continuum model. We reproduce Belavin and Polyakov's seminal work on ferromagnetic skyrmions and show how, for a particular set of analytically solvable models, common interactions present in chiral magnets set an optimal size scale for the otherwise scale-free Belavin-Polyakov skyrmions. We then numerically study the size scale of isolated skyrmions that differ slightly from the analytically solvable models for the easy-plane ferromagnet $Fe_{0.7}Co_{0.3}Si$. Lastly, we introduce a new ansatz for skyrmion profiles that reproduces the behavior of the numerical solutions equally as well as another commonly used isolated skyrmion profile.

Subsequently, we center our attention on antiferromagnets. We numerically study isolated skyrmions on chiral antiferromagnets with easy-axis anisotropy in the presence of a magnetic field. We find there is a region of phase space where isolated skyrmion solutions have a non-vanishing size and lower energy than the antiferromagnetic phase. Additionally, we observe that magnetic fields increase the stability of isolated antiferromagnetic skyrmions. Furthermore, using Monte Carlo simulations, we confirm that there is a region of phase space where antiferromagnetic skyrmions are stable configurations at finite temperatures even in the absence of a magnetic field. Finally, we observe that magnetic fields increase the size of antiferromagnetic skyrmions.

---

* Master's thesis

** Facultad Ciencias. Escuela de Física.

Introduction

Skyrmions originated as localized solutions to non-linear field theories (solitons) that, due to their non-trivial topology, had particle-like behavior. These topologically stable solitons were introduced by T. H. R. Skyrme in the 1960s to model baryons in the atomic nucleus Manton and Sutcliffe (2004). Since then, the term skyrmion has been used to identify localized and topologically non-trivial quasi-particles that have emerged in different fields of physics.

In magnetic materials, skyrmions were first predicted by Belavin and Polyakov in 1975 Belavin and Polyakov (1975) as possible metastable states of ferromagnets described by the classical isotropic Heisenberg energy functional. Later at the end of the 1980s and for more than a decade, Bogdanov and collaborators established that chiral interactions (interactions that are not symmetric under spatial inversion), present in non-centrosymmetric materials, can lead to thermodynamically stable skyrmions Bogdanov and Yablonskii (1989); Bogdanov and Hubert (1994); Bogdanov (1995); Bogdanov and Hubert (1999); Bogdanov and Rößler (2001); Rößler et al. (2006). These chiral interactions are known as Dzyaloshinskii-Moriya interactions (DMI) and tend to align spins perpendicular to each other Dzyaloshinsky (1958); Moriya (1960), in contrast to the Heisenberg exchange interaction which favors parallel spins.

Magnetic skyrmions were observed for the first time in the bulk of the chiral magnet MnSi (see Figure 2), where they could detect skyrmion spin lattices in a small region of the phase diagram known as the A-phase Muhlbauer et al. (2009). Soon after, skyrmions lattices were observed in a thin film of $Fe_{0.5}Co_{0.5}Si$ crystal, where it was identified that skyrmions can be stabilized more

easily in thin films Yu et al. (2010). After these initial observations, skyrmion lattices have been generated in many different ferromagnetic materials Everschor-Sitte et al. (2018) .

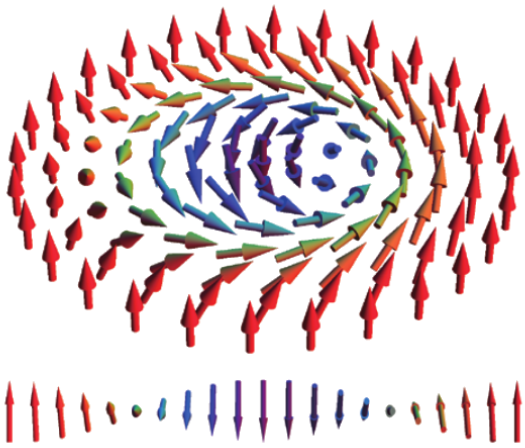

Figure 1. Magnetization distribution in an isolated skyrmion configuration. The magnetic moments rotate perpendicular to the radial direction when moving from the center to the outside. Figure taken from Kezsmarki et al. (2015).

From a theoretical perspective, the properties of ferromagnetic skyrmions have been studied extensively. Analytical approximations and numerical simulations have been shown to correctly predict the properties of isolated ferromagnetic skyrmions and ferromagnetic skyrmion lattices Nagaosa and Tokura (2013); Leonov et al. (2016); Wang et al. (2018); Göbel et al. (2021). Nonetheless, ferromagnetic skyrmions have remained an interesting topic for theoretical research, more recently thanks to the discovery of a family of exact solutions to models of easy-plane chiral ferromagnets Schroers (2019); Walton (2020); Hill et al. (2021); Ross et al. (2021).

Since their experimental observation, magnetic skyrmions have been considered candidates to act as the information carrier in future racetrack memories, due to their great stability against thermal fluctuations Zhou (2019). However, due to the existence of a skyrmion Hall effect,

skyrmions in ferromagnets exhibit unwanted behavior when moved by a spin-polarized current and can be therefore problematic for applications in data storage devices Göbel et al. (2021). Because of this, different spin textures have been proposed to avoid these shortcomings. Among these, antiferromagnetic skyrmions: skyrmions on a two-sublattice (bipartite) material in which the spins of one sublattice are reversed, are regarded as more suitable for applications in data storage due to the cancellation of the skyrmion Hall effect that occurs in these materials.

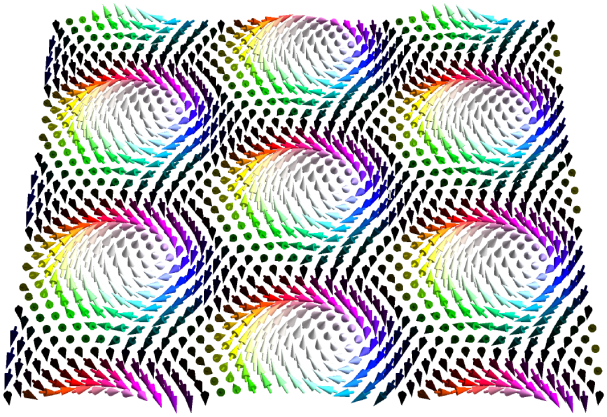

Figure 2. Skyrmion lattice like the one found in MnSi. Figure taken from Göbel (2020).

Nevertheless, there are some obstacles in creating and detecting antiferromagnetic skyrmions. Conventional techniques to generate skyrmions like spin torques or magnetic fields are not applicable to antiferromagnetic materials because they would need to be applied on each sublattice with opposite signs, which is hard to accomplish at scales of the lattice constant. To circumvent this, it has been proposed to couple the antiferromagnetic material with a collinear antiferromagnetic layer, whose magnetization can act as a staggered magnetic field Göbel et al. (2017). With regards to detection, antiferromagnetic skyrmions cannot be detected by traditional techniques due

to the local compensation of both the magnetization and the topological charge. New detection techniques are being explored to detect the topological spin Hall effect that might arise in antiferromagnetic skyrmions.

Because of these technical challenges, antiferromagnetic skyrmions have not been experimentally discovered yet. It is therefore of interest to explore the possibility of finding antiferromagnetic materials that can host antiferromagnetic skyrmions that do not requiere staggered magnetic fields.

There have been several approaches to determine the conditions under which antiferromagnetic skyrmions can form in thin films. In the triangular lattice, Rosales et al. Rosales et al. (2015) found using Monte Carlo simulations that a magnetic field induces a three-sublattice skyrmion crystal and it has subsequently been shown that single-ion anisotropies enhance the stability of this phase Mohylna et al. (2021). In the square lattice, Kessman et al. Keesman et al. (2016) showed using Monte Carlo simulations that skyrmion lattices don't form in this geometry but that isolated skyrmions can form in small finite-sized systems. Further works on micromanagement simulations of chiral antiferromagnets have confirmed Zhang et al. (2016); Bessarab et al. (2019a); Potkina et al. (2020) the stabilization of isolated antiferromagnetic skyrmions in small systems. Additionally, they have found that magnetic fields increase the stability of antiferromagnetic skyrmions. Despite this, a full phase diagram that includes temperature dependence showing where antiferromagnetic skyrmions can form has not been presented.

This thesis will be divided into two big themes: the analytical analysis of skyrmion solutions in chiral ferromagnets and the simulation of chiral antiferromagnets with the purpose of finding

stable skyrmion phases. In Chapter 1 we will introduce the continuous and discrete theoretical models of chiral magnets that will be used throughout the thesis, as well as the necessary numerical methods needed to calculate the ground states for these models. In Chapter 2 we will focus on the analytical analysis of isolated ferromagnetic skyrmions in the continuum approximation. We reproduce the original work in magnetic skyrmions by Bleavin and Polyakov. We then study the size of skyrmions on chiral ferromagnets using a variational method and turn to numerical solutions to complete the analysis. Furthermore, we propose a new trial function for skyrmion profiles and evaluate how well it approximates the numerical solutions. In Chapter 3, we will focus on the simulation of chiral antiferromagnets. We study the stability of isolated skyrmions using a continuum model. Then we use Monte Carlo simulations to construct the phase diagram of the discrete model of a chiral ferromagnet in the square lattice. We explore the effects of magnetic fields and temperature on the different phases that we found. In the concluding Chapter 4, we summarize the obtained results and put forward possible extensions of the work presented here.

1. Theoretical and numerical methods

Magnetic materials are materials that have a net magnetic moment at the atomic level. A full description of a magnetic material is a many-body quantum mechanical problem but a full quantum mechanical treatment is computationally challenging. Since the phenomena we are interested in can be observed on a classical level, we can ignore quantum fluctuations and model this many-body system classically. In this chapter, we will introduce the discrete and continuum classical spin models which are used in this thesis to describe magnetic materials. Since the Hamiltonian of a magnetic material consists of multiple magnetic interaction terms which give rise to rich and complex physical phenomena, there are in general no exact analytical solutions available. For this reason, approximate analytical or numerical methods are essential to study these systems. We present a detailed description of the numerical methods we used to study both discrete and continuum classical spin systems.

1.1. Discrete model

A discrete classical spin model (commonly referred to as a classical Heisenberg model) assumes each ion i in a magnetic material carries a net magnetic moment represented by a three-dimensional unit vector $\mathbf{S}_i = \mu_i/\|\mu_i\|$ where μ_i is the atomic magnetic moment at site i. Given our interest in systems where magnetic skyrmions can be stabilized, in this thesis, we will consider the following Hamiltonian

$$\mathscr{H} = \mathscr{H}_{\text{exc}} + \mathscr{H}_{\text{DMI}} + \mathscr{H}_{\text{anis}} + \mathscr{H}_{\text{field}}, \tag{1}$$

where $\mathscr{H}_{\text{exc}}$ is the Heisenberg exchange interaction, $\mathscr{H}_{\text{DMI}}$ is the Dzyalonshinskii-Moriya interaction, $\mathscr{H}_{\text{anis}}$ is the uniaxial anisotropy and $\mathscr{H}_{\text{field}}$ is the interaction with an external magnetic field. In the following, we will give a short explanation of each term.

Exchange interaction. The exchange interaction is a short-range quantum effect introduced by Heisenberg to explain the long-range ordering of atomic magnetic moments in ferromagnetic materials Lévy (2000). In the classical limit, the energy due to the exchange interaction of all the magnetic moments is given by

$$\mathscr{H}_{\text{exc}} = -\sum_{\langle i,j \rangle} J_{ij}\, \mathbf{S}_i \cdot \mathbf{S}_j, \tag{2}$$

where $\sum_{\langle i,j \rangle}$ represents the sum over nearest-neighbor magnetic moments, J_{ij} is the interaction strength between two neighboring magnetic moments $\mathbf{S}_i$ and $\mathbf{S}_j$, and $\cdot$ denotes the standard dot product. For $J_{ij} > 0$ the ferromagnetic state (all magnetic moments are parallel) is favored while for $J_{ij} < 0$ the antiferromagnetic state (neighboring magnetic moments are anti-parallel) is favored.

It is common to write the exchange energy in matrix form as

$$\mathscr{H}_{\text{exc}} = -\sum_{\langle i,j \rangle} \mathbf{S}_i \mathfrak{J}_{ij} \mathbf{S}_j \quad \text{with} \quad \mathfrak{J}_{ij} = \begin{pmatrix} J_{ij} & 0 & 0 \\ 0 & J_{ij} & 0 \\ 0 & 0 & J_{ij} \end{pmatrix}, \tag{3}$$

where its symmetric nature is highlighted.

Dzyalonshinskii-Moriya interaction. The Dzyalonshinskii-Moriya interaction is an antisymmetrical interaction present in some non-centrosymmetric magnets and interfacially asymmetric multilayers that in the classical Heisenberg model can be written as Jiang et al. (2017b)

$$\mathscr{H}_{\mathrm{DMI}} = \sum_{\langle i,j \rangle} \mathbf{D}_{ij} \cdot (\mathbf{S}_i \times \mathbf{S}_j), \tag{4}$$

where $\mathbf{D}_{ij}$ is the Dzyaloshinskii-Moriya vector corresponding to the interaction of two neighboring magnetic moments $\mathbf{S}_i$ and $\mathbf{S}_j$, which is dictated by the symmetry of the material or stack of materials; and $\times$ denotes the standard cross product. This interaction, in contrast to Heisenbergs' exchange interaction, favors the perpendicular alignment of neighboring magnetic moments and has been shown effective at stabilizing skyrmion structures.

In a similar fashion to the exchange energy, the DMI energy can be written in matrix form as

$$\mathscr{H}_{\mathrm{DMI}} = -\sum_{\langle i,j \rangle} \mathbf{S}_i \mathfrak{D}_{ij} \mathbf{S}_j \quad \text{with} \quad \mathfrak{D}_{ij} = \begin{pmatrix} 0 & \mathrm{D}_{ij}^{z} & -\mathrm{D}_{ij}^{y} \\ -\mathrm{D}_{ij}^{z} & 0 & \mathrm{D}_{ij}^{x} \\ \mathrm{D}_{ij}^{y} & -\mathrm{D}_{ij}^{x} & 0 \end{pmatrix}, \tag{5}$$

where its antisymmetric nature is highlighted.

Uniaxial anisotropy. In magnetic materials, the magnetization can have one or many preferred axes, commonly known as easy axes. The contribution of this on-site effect to

the energy is given by

$$\mathscr{H}_{\text{anis}} = -K\sum_i (\mathbf{S}_i \cdot \hat{\nu})^2 , \tag{6}$$

where K is the magnitude of the anisotropy (easy-axis for $K > 0$ and easy-plane for $K < 0$) and $\hat{\nu}$ is the easy or hard axis.

Interaction with an external field. The energy describing the classical interaction of the moments with a uniform external magnetic field (sometimes called Zeeman energy) is given by

$$\mathscr{H}_{\text{field}} = -\sum_i \mathbf{B}_i \cdot \mathbf{S}_i, \tag{7}$$

where $\mathbf{B}_i = \|\mu_i\|\mathbf{b}_i$ and $\mathbf{b}_i$ is the magnetic field at site i.

1.1.1. Numerical methods for discrete models. To calculate equilibrium quantities like the magnetization or magnetic susceptibility, the standard analytical procedure consists in calculating the partition function of our model, given in the canonical ensemble by Joyce (1967)

$$Z = \int_{\Omega_1} \ldots \int_{\Omega_N} \prod_{i=1}^{N} \frac{d\Omega_i}{4\pi} \exp\{-\beta\mathscr{H}\}, \tag{8}$$

where $d\Omega_i$ is the element of solid angle in the direction $\mathbf{S}_i$. With Z, all thermodynamic quantities can be found by taking derivatives with respect to the parameters of the system. Nevertheless, the high dimensional integral appearing in Z can only be solved exactly in some special cases. Alternatively, approximations like the mean-field approximation, or computational methods like the Monte Carlo method have to be used.

In this thesis, we will use Monte Carlo methods to simulate discrete systems and calculate equilibrium quantities. In Monte Carlo simulations, the goal is to avoid calculating thermodynamic quantities via the partition function but rather to compute averages directly using a procedure known as importance sampling. The idea behind importance sampling is to choose a subset of states at random from a probability distribution $q(\mu)$, where μ is the state of the system, in such a way that we include the important areas in the phase space of the system.

Suppose we want to find the expectation value of a physical quantity Q, in the canonical ensemble this is given by

$$\langle Q \rangle = \int_{\Omega_1} ... \int_{\Omega_N} \prod_{i=1}^{N} \frac{d\Omega_i}{4\pi} Q(\mu)\, p(\mu), \tag{9}$$

where $p(\mu) = \frac{1}{Z} \exp\{-\beta \mathscr{H}(\mu)\}$. We can introduce importance sampling (if $q(\mu) \neq 0 \, \forall \mu$) in the following manner

$$\langle Q \rangle = \int_{\Omega_1} ... \int_{\Omega_N} \prod_{i=1}^{N} \frac{d\Omega_i}{4\pi} Q(\mu)\, p(\mu) \frac{q(\mu)}{q(\mu)} = \left\langle Q \frac{p(\mu)}{q(\mu)} \right\rangle_q . \tag{10}$$

This way, if we choose $q(\mu) = p(\mu)$ we have $\langle Q \rangle = \langle Q \rangle_q$ and a sample of states $\{\mu_1, ..., \mu_M\}$ drawn from $q(\mu)$ can be used to estimate $\langle Q \rangle$ by

$$\langle Q \rangle \simeq \frac{1}{M} \sum_{i=1}^{M} Q(\mu_i). \tag{11}$$

This approach allows us to compute expectation values using a small number of states,

namely, the most likely states according to the canonical distribution.

1.1.1.1. Metropolis-Hastings algorithm. The remaining part of the method consists in finding a way to pick a sample of states whose distribution is the canonical distribution. There exists different algorithms that accomplish this, the most widely known being the Metropolis-Hastings algorithm. To sample from the canonical distribution, the Metropolis-Hastings algorithm starts by initializing the system in some state μ_n. Then repeating the following steps until convergence Kroese et al. (2011):

1. Generate a new configuration ν.
2. Calculate the energy difference between the two states ΔE.
3. Generate a random number $r \in [0,1]$.
4. Choose the new state of the system according to

$$\mu_{n+1} = \begin{cases} \nu & \text{if } r \leq \min\left(\mathrm{e}^{-\beta \Delta \mathrm{E}}, 1\right) \\ \mu_n & \text{otherwise.} \end{cases}$$

This group of steps constitutes a Monte Carlo step. This algorithm always accepts changes if the new configuration lowers the total energy of the system. Additionally, when a new configuration has higher energy it still has a chance of being accepted, with a probability given by the Boltzmann factor of the energy difference.

In each iteration of the process, the generation of a new configuration is done following an update algorithm. For a three-dimensional spin variable, the most widely used update algorithm consists in choosing a random orientation for the spin in such a way that the distribution of spins over the unit sphere is uniform. One way of doing this Newman and Barkema (1999) is to choose two uniformly distributed numbers $r_1, r_2 \in [0,1]$, calculate the angle coordinates according to

$$\phi = 2\pi r_1, \quad \theta = \cos^{-1}(2r_2 - 1) \tag{12}$$

and then transform this to Cartesian coordinates using the fact that

$$\mathbf{S} = (\sin\theta\cos\phi, \sin\theta\sin\phi, \cos\theta). \tag{13}$$

This update algorithm takes into account that the element of solid angle depends on the polar angle θ: $d\Omega = \sin\theta d\theta d\phi$, making the distribution of θ non-uniform.

Figure 3 presents a comparison between the sampling of orientations on the unit sphere following the presented algorithm and other algorithms that do not sample the unit sphere uniformly.

1.1.1.2. Parallel tempering. Hamiltonians with continuous spin variables and many interactions like the one we are considering (Eq. (1)) have complex energy landscapes with multiple local minima. These local minima are separated by energy barriers which, at low temperatures, can trap the system in metastable states. To overcome these energy barriers and ensure a global energy minimum is reached, we complement the Metropolis-Hastings algorithm with the parallel

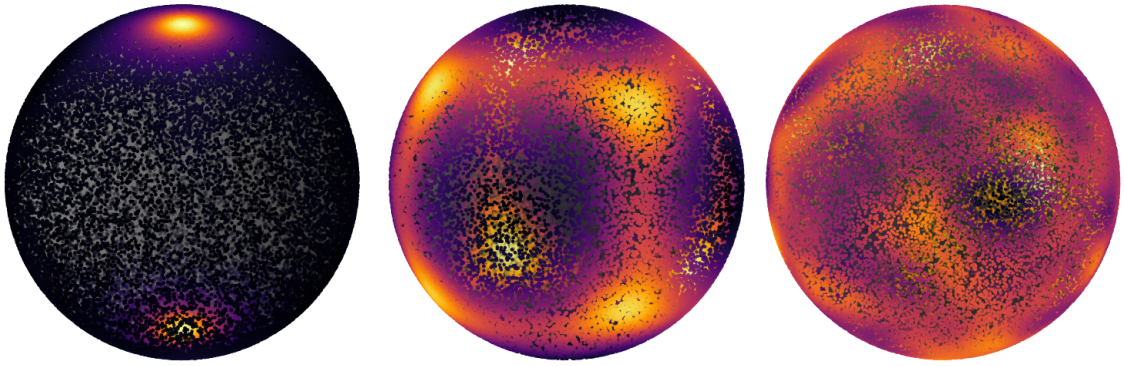

(a) (b) (c)

Figure 3. Comparison between non-uniform and uniform sampling of 40.000 points over the unit sphere, color represents point density. **(a)** Sampling done by choosing a uniform distribution for the spherical angles $\phi \in [0, 2\pi]$ and $\theta \in [0, \pi]$, and transforming Cartesian coordinates. **(b)** Sampling done by choosing the Cartesian coordinates between $[-1.0, 1.0]$ at random and normalizing. **(c)** Sampling done by choosing the angular variables according to 12 and transforming Cartesian coordinates.

tempering algorithm.

The parallel tempering algorithm consists in simulating multiple replicas of the same system at different temperatures $\{T_0, T_1, ..., T_{N-1}\}$ and making an exchange between neighboring replicas after some number of Metropolis-Hastings Monte Carlo steps. This exchange induces a random walk of the replicas along temperature space, allowing replicas at low temperatures to move to a high-temperature region, where energy barriers can be easily overcome, and back to low temperatures.

The replica exchange between two neighboring replicas with temperatures T_n, T_m is done by repeating the following steps Hukushima and Nemoto (1996):

1. Calculate the quantity $\Delta = (\beta_n - \beta_m)(E_m - E_n)$.

2. Generate a random number $p \in [0, 1]$

3. Exchange replicas if $p \leq \min\left(e^{-\Delta}, 1\right)$.

The performance of the parallel tempering algorithm is heavily influenced by the choice of temperatures $\{T_0, T_1, ..., T_{N-1}\}$. To optimize our choice of temperatures, we follow the recursive method presented in reference Berg (2004). We start by choosing a wide, evenly spaced set of inverse temperatures $\{\beta_1^0, \beta_2^0, ..., \beta_{N-1}^0\}$ and, after certain amount of Monte Carlo steps, obtaining a new set of inverse temperatures that optimize the number of accepted exchanges according to

$$\beta_0^{m+1} = \beta_0^m \quad \text{and} \quad \beta_i^{m+1} = \beta_{i-1}^{m+1} + a_i^m(\beta_i^m - \beta_{i-1}^m) \qquad \text{for} \quad i = 1, ..., N-1, \tag{14}$$

where

$$a_i^m = \lambda^m a_i^{pt,m} \quad \text{with} \tag{15}$$

with

$$\lambda^m = \frac{\beta_{N-1}^m - \beta_0^m}{\sum_i^{N-1} a_i^{pt,m}(\beta_i^m - \beta_{i-1}^m)}, \tag{16}$$

and $a_i^{pt,m}$ is the acceptance rate of the exchange between replicas $i-1$ and i. This is carried out recursively until the acceptance rate between replicas is between $0.3 - 0.9$.

After the simulation reaches equilibrium, an extra amount of Monte Carlo steps are performed to calculate statistical averages of the desired physical quantities using the estimator (11).

1.1.2. Classifying phases. To identify the phase of the equilibrium spin configuration, we define two useful quantities: the static spin structure factor and the skyrmion number of the configuration.

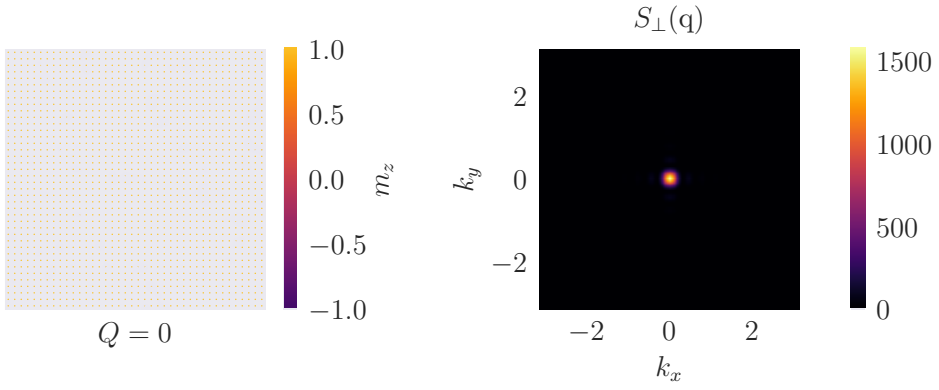

(a)

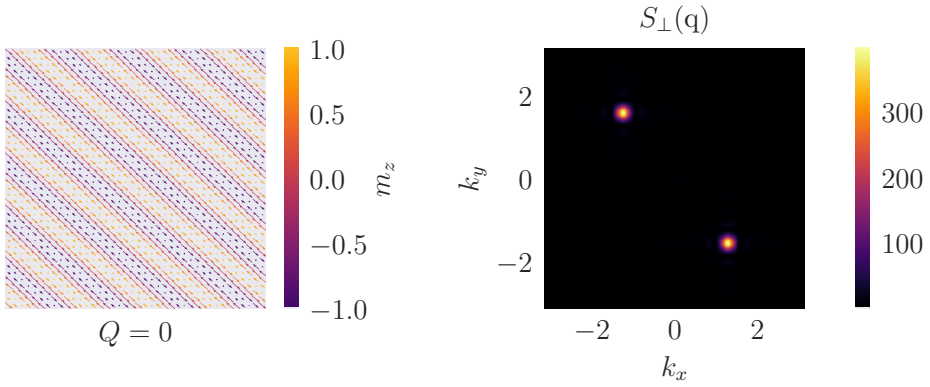

(b)

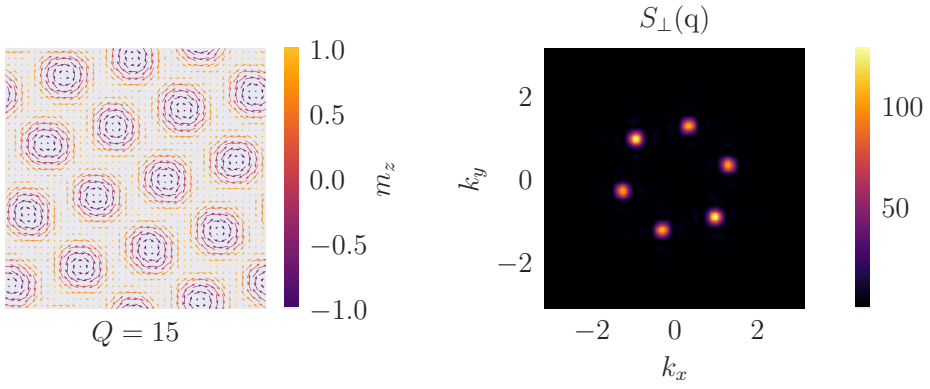

(c)

Figure 4. Real space spin configurations, topological charge and spin structure factor for different multiple-q structures for a ferromagnetic Heisenberg model in the square lattice. These three pieces of information are key when constructing magnetic phase diagrams. (a) Ferromagnetic phase. (b) Spiral phase. (c) Skyrmion phase. Simulations reproduced from Gómez Albarracín and Rosales (2022).

1.1.2.1. Spin structure factor. The static spin structure factor is the Fourier transform of the two-point correlation function and can be calculated as

$$S(\mathbf{q}) = \frac{1}{N}\langle|\sum_i \mathbf{S}_i e^{-i\mathbf{q}\cdot\mathbf{r}_i}|^2\rangle,$$

where N is the total number of spins and $\langle\rangle$ represents the average over different Monte Carlo configurations. In the presence of a magnetic field or materials with single-ion anisotropy, it is convenient to calculate the structure factor in the parallel and perpendicular directions to the preferred axis (assumed here as the z-axis) separately

$$S_{\parallel}(\mathbf{q}) = \frac{1}{N}\langle|\sum_i S_i^z e^{-i\mathbf{q}\cdot\mathbf{r}_i}|^2\rangle \tag{17}$$

$$S_{\perp}(\mathbf{q}) = \frac{1}{N}\langle|\sum_i S_i^x e^{-i\mathbf{q}\cdot\mathbf{r}_i}|^2 + \sum_i S_i^y e^{-i\mathbf{q}\cdot\mathbf{r}_i}|^2\rangle. \tag{18}$$

Peaks in the spin structure factor will correspond to the propagation vectors $\mathbf{q}$ appearing in the Fourier expansion of the spin distribution

$$\mathbf{S}_i = \sum_{\mathbf{q}} \mathbf{S}_{\mathbf{q},i} e^{-i\mathbf{q}\cdot\mathbf{r}_i}. \tag{19}$$

Because $\mathbf{S}_i$ is real, each propagation vector appears in pairs $\pm\mathbf{q}$ in the Fourier expansion, except for $\mathbf{q} = 0$. Due to the periodicity of the lattice, the propagation vectors are periodical in reciprocal space and we can restrict the calculation of the spin structure factors to the first Brillouin zone.

The amount of independent peaks in the spin structure factor (amount of independent propagation vectors present in expansion (19)) is used to classify the magnetic structure: one independent peak represents a single-q structure, two independent peaks a double-q structure and, so on. The specific structure will depend on the type of lattice, in Figure 4 we show the real space spin configuration and the spin structure factor for different ferromagnetic multi-q structures in the square lattice.

1.1.2.2. Skyrmion number. For skyrmions in the continuous picture, the winding number (also called topological charge) of a magnetization configuration $\mathbf{m}(\mathbf{r})$ is given by Göbel et al. (2021)

$$Q = \frac{1}{4\pi}\int \mathbf{m}(\mathbf{r}) \cdot \left[\frac{\partial \mathbf{m}(\mathbf{r})}{\partial x} \times \frac{\partial \mathbf{m}(\mathbf{r})}{\partial y}\right] dxdy = 0, \pm 1, \pm 2, ... \tag{20}$$

allowing only integer topological charges for the different types of skyrmions.

Expression (20) can be adapted to the discrete atomistic model. This was done by Berg and Lüscher in Berg and Lüscher (1981). In the square lattice, the topological charge density q_l defined in a unit cell of the lattice is given by Böttcher et al. (2018)

$$A_i = A_i^{(12)}\text{sign}[\chi_\text{i}^{(12)}] + \text{A}_\text{i}^{(34)}\text{sign}[\chi_\text{i}^{(34)}], \tag{21}$$

where $A_i^{(ab)} = \|(\mathbf{S}_a - \mathbf{S}_i) \times (\mathbf{S}_b - \mathbf{S}_i)\|/2$ is the the area of the surface spanned by the spins in the elementary triangle $\mathbf{S}_i$, $\mathbf{S}_a$ and $\mathbf{S}_b$; $\chi_i^{(ab)} = \mathbf{S}_i \cdot (\mathbf{S}_a \times \mathbf{S}_b)$ and $\mathbf{S}_1$, $\mathbf{S}_2$, $\mathbf{S}_3$, $\mathbf{S}_4$ are $\mathbf{S}_i$'s nearest-neighbor spins (see Figure 5).

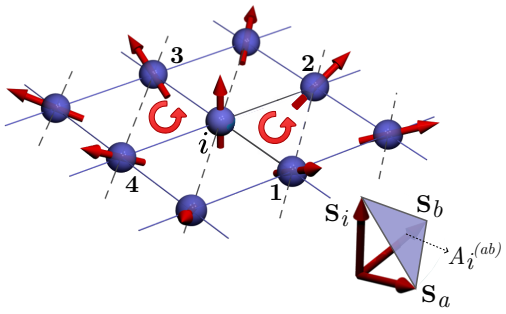

Figure 5. Illustration of the quantities involved in the calculation of the topological charge in the square lattice (Eq. 21).

The total topological charge of the lattice is found by summing over all sites in the lattice

$$Q = \frac{1}{4\pi}\sum_i A_i. \tag{22}$$

1.2. Continuum model

For ferromagnetic materials, if we assume the magnetic moments in the material vary in a length scale that is large compared with inter-atomic distances, we can approximate the spin configuration by a continuous magnetization field $\mathbf{m}(\mathbf{r})$ which takes the value of the spin S_i on the position of the lattice site $\mathbf{r}_i$. The Hamiltonian then becomes an energy functional of the magnetization (see Appendix 1 for a derivation from the discrete model)

$$F[\mathbf{m}] = \int_{\mathbb{R}^3} \left[\mathscr{J}\,(\partial_\mu \mathbf{m})^2 + \mathscr{D}\mathbf{m}\cdot(\nabla\times\mathbf{m}) - \mathscr{K}\,m_3^2 - M_s B m_3\right] d^3x, \tag{23}$$

where $\mathscr{D}$ is the DMI strength, $\mathscr{K}$ is the magnitude of a single-ion anisotropy (easy-axis for $\mathscr{K} > 0$ and easy-plane for $\mathscr{K} < 0$), M_s is the saturation magnetization and B is the magnitude of an

external magnetic field applied in the x_3 direction.

For antiferromagnetic materials ($J_{ij} < 0$ in Equation (2)) energy functional (23) is slightly changed. Neighboring magnetic moments tend to be anti-parallel and it is natural to describe the system as a bipartite lattice. In a bipartite lattice (like the square or honeycomb lattices) the sites can be divided into two sublattices where sites in one sublattice only interact with sites in the other sublattice. If we label the sublattices of a square lattice as a and b, we can map an antiferromagnetic configuration into a ferromagnetic configuration by inverting the direction in one of the sublattices $\mathbf{S}_i^b \mapsto -\mathbf{S}_i^b$ (see Figure 6).

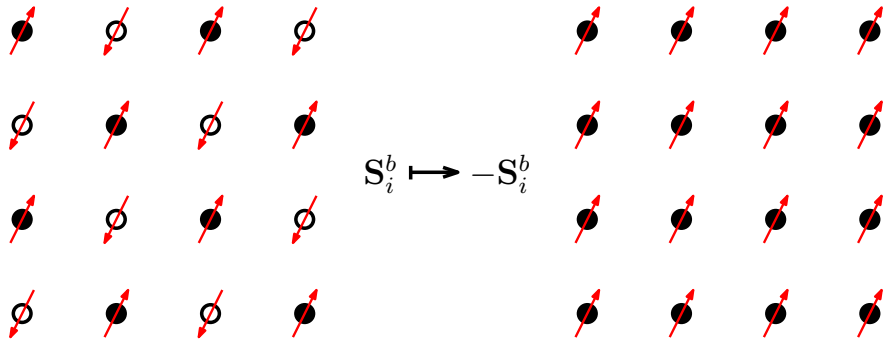

Figure 6. Mapping between antiferromagnetic and ferromagnetic systems allowed by the bipartite nature of the square lattice.

If we change the Hamiltonian parameters as $J_{ij} \mapsto -J_{ij}$ and $\mathbf{D}_{ij} \mapsto -\mathbf{D}_{ij}$, it can be shown Keesman et al. (2016) that the continuum energy functional becomes

$$F_{\mathrm{AF}}[\mathbf{m}] = \int_{\mathbb{R}^3} \left[\mathscr{J}\,(\partial_\mu \mathbf{m})^2 + \mathscr{D}\mathbf{m} \cdot (\nabla \times \mathbf{m}) - \mathscr{K} m_3^2 + \frac{(M_s B)^2}{32A}(m_3^2 - 1) \right] d^3x. \tag{24}$$

In the following, we will only consider the ferromagnetic energy functional (23) as an example, but the procedure for the antiferromagnetic energy functional (24) is analogous.

Expanding the magnetization as

$$\mathbf{m}(x_1,x_2) = (\cos\phi\sin\theta, \sin\phi\sin\theta, \cos\theta), \tag{25}$$

and considering axisymmetric spin configurations $\theta = \theta(\rho)$ in a thin film, we can put energy functional 23 in the standard form Leonov et al. (2016)

$$F[\theta(\rho)] = 2\pi\int_0^\infty \left[\mathscr{J}\left(\left(\frac{d\theta}{d\rho}\right)^2 + \frac{\sin^2\theta}{\rho^2}\right) + \mathscr{D}\left(\frac{d\theta}{d\rho} + \frac{\sin(2\theta)}{2\rho}\right) + \mathscr{K}\sin^2\theta + M_s B(1-\cos\theta)\right]\rho\, d\rho. \tag{26}$$

The Euler-Lagrange equation associated with energy functional (26) equation reads

$$\mathscr{J}\left(\frac{d^2\theta}{d\rho^2} + \frac{1}{\rho}\frac{d\theta}{d\rho} + \frac{\sin(2\theta)}{2\rho^2}\right) + \mathscr{D}\frac{\sin^2\theta}{\rho} - \mathscr{K}\frac{\sin(2\theta)}{2} - M_s B\sin(\theta) = 0, \tag{27}$$

and isolated skyrmion solutions to Eq. (27) satisfy boundary conditions

$$\theta(0) = \pi \qquad \text{and} \qquad \theta(\infty) = 0. \tag{28}$$

1.2.1. Numerical methods for continuum models. There are no known analytical solutions to Eq. (27) subject to boundary conditions (28) for arbitrary values of $\mathscr{J}$, $\mathscr{D}$, $\mathscr{K}$, M_s and B. Consequently, numerical approximations are necessary.

We start by introducing the dimensionless variables

$$r = \frac{\rho}{\rho_0}, \qquad k = \frac{\mathscr{K}}{K_0}, \qquad h = \frac{\mathscr{B}}{H_0} \tag{29}$$

where

$$\rho_0 = \frac{\mathscr{J}}{\mathscr{D}}, \qquad K_0 = \frac{\mathscr{D}^2}{\mathscr{J}}, \qquad H_0 = \frac{\mathscr{D}^2}{\mathscr{J} M_s}. \tag{30}$$

In terms of which the energy functional and Euler-Lagrange equation takes the form

$$\frac{F[\theta(r)]}{2\pi\mathscr{J}} = \int_0^\infty \left[\left(\left(\frac{d\theta}{dr} \right)^2 + \frac{\sin^2\theta}{r^2} \right) + \left(\frac{d\theta}{dr} + \frac{\sin(2\theta)}{2r} \right) + k\sin^2\theta + h(1-\cos\theta) \right] r dr. \tag{31}$$

and

$$\left(\frac{d^2\theta}{dr^2} + \frac{1}{r}\frac{d\theta}{dr} + \frac{\sin(2\theta)}{2r^2} \right) + \frac{\sin^2\theta}{r} - k\frac{\sin(2\theta)}{2} - h\sin(\theta) = 0. \tag{32}$$

Next, we map the semi-infinite domain $r \in [0,\infty)$ to a finite domain $x \in (0,1]$ introducing the change of variables

$$r = \frac{1-\sqrt{x}}{\sqrt{x}} \quad \longrightarrow \quad \frac{d\theta}{dr} = -2x^{3/2}\frac{d\theta}{dx}. \tag{33}$$

Inserting (33) into (31) and (32) results in

$$\frac{F}{2\pi\mathscr{J}} = \int_0^1 \Bigg[4x^3 \left(\frac{d\theta}{dr}\right)^2 + \frac{x}{(1-\sqrt{x})^2}\sin^2\theta + \left(-2x^{3/2}\frac{d\theta}{dr} + \frac{\sqrt{x}}{2(1-\sqrt{x})}\sin(2\theta)\right) + k\sin^2\theta + h(1-\cos\theta)\Bigg]\frac{(1-\sqrt{x})}{2x^2}dx \tag{34}$$

and

$$4x^3\frac{d^2\theta}{dx^2} + x^2\left(\frac{3}{2} - \frac{1}{1-\sqrt{x}}\right)\frac{d\theta}{dx} - \frac{x}{2(1-\sqrt{x})}\sin 2\theta + \frac{\sqrt{x}}{1-\sqrt{x}}\sin^2\theta - k\sin\theta(1-\cos\theta) - h\sin\theta = 0, \tag{35}$$

with boundary conditions

$$\theta(x=0) = 0 \qquad \text{and} \qquad \theta(x=1) = \pi. \tag{36}$$

To find solutions $\theta(x)$ to Eq. (35) subject to boundary conditions (36), instead of using finite-element methods, we can treat this as a minimization problem. Expanding the magnetization profile as a Fourier series we use the Fourier coefficients as parameters to minimize energy functional 34 using a Monte Carlo-type method.

We make the Fourier expansion of the magnetization profile as

$$\theta(x) = \pi x + \sum_{n=1}^{n_{\max}} c_n \sin(n\pi x), \tag{37}$$

which satisfies boundary conditions (36). Minimization of (34) was done by initializing the first sixty Fourier coefficients ($n_{\max} = 60$) to zero and repeating the following steps until convergence

1. Assign c_1 randomly between $[-\pi, \pi]$.

2. Calculate the new energy by numerically integrating (34).

3. If the energy is lowered and $0 \leq \theta(x) \leq \pi$ for every $x \in [0,1]$, accept the change. Else, revert the change.

4. Repeat for all coefficients.

After the algorithm has converged to a set of Fourier coefficients, its energy is stored and the resulting *optimal* magnetization profile is recovered using Equation 37. One of the main features of the magnetization profile we are interested in is the size of the isolated skyrmion. We characterize the skyrmion size by the radius of the skyrmion profile which we define as the distance R at which the spins are laying in the *xy* plane:

$$R = r(\theta = \pi/2). \tag{38}$$

1.3. Summary

We have presented the theoretical and numerical tools upon which the following chapters will be built on. In Section 1.1 we introduced the classical Heisenberg model we will use to model square lattice chiral antiferromagnets in Chapter 3. In Section 1.1.1 we explained the Metropolis-Hastings Monte Carlo method along with the parallel tempering algorithm, which was our method of choice to find the ground state and study the thermodynamic quantities of the classical Heisenberg model. We used the implementation of the library SpinMC.jl Buessen (2021) as the starting point due to its flexibility, then we added the optimization of the temperatures for the parallel tem-

pering algorithm and the calculation of the quantities necessary for phase identification. In Section 1.2 we introduced the continuum version of the classical Heisenberg model for both ferromagnets and antiferromagnets that we will use in Chapters 2 and 3, respectively. In Section 1.2.1 we put forward a stochastic method to solve the non-linear ordinary differential equation that governs isolated skyrmion profiles in chiral magnets.

2. Isolated ferromagnetic skyrmions

Ferromagnetic skyrmions were the first kind of magnetic skyrmions to be theoretically predicted and experimentally observed. As such, many of their properties have been studied in detail. In this chapter, we discuss known theoretical facts about isolated ferromagnetic skyrmions which have been found to be useful to describe the properties of isolated skyrmions observed in experiments Leonov et al. (2016); Wang et al. (2018). First, we reproduce the first theoretical prediction of magnetic skyrmions by Belavin and Polyakov as a tool to introduce the topological features of magnetic skyrmions. Next, we explore skyrmions solutions in easy plane chiral ferromagnets where it has been shown skyrmions equal to those predicted by Belavin and Polyakov exist for a certain choice of physical parameters. We compute numerical skyrmion solutions that differ slightly from this special choice of parameters and study the dependence of their size on the magnetic field applied. Finally, we propose a new skyrmion profile ansatz by adding a cut-off to the Belavin-Polyakov skyrmion solution and evaluate how well can it fit the numerical solutions obtained previously.

2.1. Belavin-Polyakov skyrmions

At low temperatures and large scales, the interaction of the spins of an isotropic two-dimensional FM can be described in the continuum limit by the energy functional

$$F[\mathbf{m}(x_1,x_2)] = \int_{\mathbb{R}^2} \mathscr{J}\,(\partial_\mu \mathbf{m})^2 d^2x = \int_{\mathbb{R}^2} \mathscr{J} \sum_\mu (\partial_\mu \mathbf{m})\cdot(\partial_\mu \mathbf{m}) d^2x \qquad (\mu = 1,2), \tag{39}$$

where A is the exchange constant of the material and $\mathbf{m}(x_1, x_2)$ is a unit vector that represents the magnetization field.

Energy functional (39) has a global minimum for $\mathbf{m} = \text{const}$ which is the trivial ferromagnetic configuration. Nonetheless, Belavin and Polyakov demonstrated Belavin and Polyakov (1975) the existence of non-trivial local minima of (39) with particle-like properties. In the following, we will go through the derivation of these non-trivial configurations.

First, we will present the topological arguments that lead to the possibility of such configurations. Expressing the magnetization field in terms of spherical coordinates as

$$\mathbf{m}(x_1, x_2) = (\cos\phi \sin\theta, \sin\phi \sin\theta, \cos\theta), \tag{40}$$

which are the coordinates of a point in a 2-sphere, we can see that $\mathbf{m}$ is a map $\mathbb{R}^2 \mapsto S^2$. Furthermore, for the energy of the configuration to be finite, $\mathbf{m}$ has to be constant at spatial infinity, say

$$\mathbf{m}(x_1, x_2) \to (1, 0, 0) \qquad \text{as} \qquad \rho = \sqrt{x_1^2 + x_2^2} \to \infty. \tag{41}$$

This allows us to view spatial infinity as one point and our x, y plane becomes topologically equivalent to a sphere (via a stereographic projection). Therefore, the magnetization vector defines a map $\mathbf{m} : S^2 \mapsto S^2$.

In topology, two maps are homotopy equivalent if they can be continuously deformed into each other. Accordingly, we can classify maps by homotopy classes: collections of maps that are homotopy equivalent to each other. For $S^2 \mapsto S^2$ maps, the homotopy classes can be uniquely

characterized by an integer Q known as the topological charge of the map, defined as

$$Q = \frac{1}{8\pi}\int_{\mathbb{R}^2} \mathbf{m}\cdot\varepsilon_{\mu\nu}(\partial_\mu\mathbf{m}\times\partial_\nu\mathbf{m})d^2x = \frac{1}{4\pi}\int_{\mathbb{R}^2}\mathbf{m}\cdot[\partial_1\mathbf{m}\times\partial_2\mathbf{m}]\,d^2x = 0,\pm1,\pm2,\ldots. \tag{42}$$

This means the space of field configurations satisfying condition (41) are divided into topological sectors characterized by the topological charge Q. To find minima of (39) in a given topological sector we use the following identity Polyakov (1987)

$$\frac{1}{2}\int_{\mathbb{R}^2}\left(\partial_\mu\mathbf{m}\pm\varepsilon_{\mu\nu}\mathbf{m}\times\partial_\nu\mathbf{m}\right)^2 d^2x = \int_{\mathbb{R}^2}(\partial_\mu\mathbf{m})^2 d^2x \mp \int_{\mathbb{R}^2}\mathbf{m}\cdot\varepsilon_{\mu\nu}(\partial_\mu\mathbf{m}\times\partial_\nu\mathbf{m})d^2x, \tag{43}$$

which allows us to calculate the energy of a spin configuration in terms of the topological charge (42) as

$$F[\mathbf{m}(x_1,x_2)] = \pm 8\pi\mathscr{J}Q + \frac{\mathscr{J}}{2}\int_{\mathbb{R}^2}\left(\partial_\mu\mathbf{m}\pm\varepsilon_{\mu\nu}\mathbf{m}\times\partial_\nu\mathbf{m}\right)^2 d^2x, \tag{44}$$

where to keep the energy positive, the $+$ sign ($-$ sign) is to be taken if $Q>0$ ($Q<0$). Equation (44) tells us that a magnetization field in a given topological sector minimizes the energy functional with energy

$$F[\mathbf{m}(x_1,x_2)] = 8\pi\mathscr{J}|Q|, \tag{45}$$

if it satisfies

$$\partial_\mu\mathbf{m} = \mp\varepsilon_{\mu\nu}\mathbf{m}\times\partial_\nu\mathbf{m}. \tag{46}$$

To solve the system of equations (46) (assuming the negative sign, corresponding to $Q>0$) it is

useful to introduce a complex variable and a complex field w such that

$$z = x_1 + ix_2, \qquad w = \frac{m_1 + im_2}{1 + m_3} = \cot\frac{\theta}{2} e^{i\phi}. \tag{47}$$

In terms of these, we can find that (46) reduces to

$$\partial_{\bar{z}} w = 0, \tag{48}$$

where $\partial_z = \frac{1}{2}(\partial_1 - i\partial_2), \partial_{\bar{z}} = \frac{1}{2}(\partial_1 + i\partial_2)$ are the complex-valued partial derivatives. Equation (48) is equivalent to the Cauchy-Riemann equations for the real and imaginary parts of w and has holomorphic functions $w(z)$ as solutions. Isolated skyrmion solutions have the form

$$w(z) = \left(\frac{z - z_0}{R_0}\right)^Q, \tag{49}$$

where z_0 is a complex number that indicates the position of the center of the skyrmion profile, R_0 is a complex number whose magnitude and phase represent the size and helicity of the skyrmion respectively.

Given z_0, R_0 and Q we can find $\mathbf{m}$ in $(x_,x_2)$ coordinates using the inverse relations

$$m_1 = \frac{w + \bar{w}}{1 + |w|^2}, \quad m_2 = \frac{1}{i}\frac{w - \bar{w}}{1 + |w|^2}, \quad m_3 = \frac{1 - |w|^2}{1 + |w|^2}. \tag{50}$$

In Figure 7 we show an example of two isolated Belavin-Polyakov skyrmions with different helic-

ities.

In this continuum approximation, a transition between spin configurations in different topological sectors would involve making a discontinuous change in the magnetization field (because they're not homotopy equivalent) which requires an infinite change in energy. Because of this, skyrmion configurations are said to be topologically protected.

A key feature of the Belavin-Polyakov skyrmion (49) is that the size R_0 is a free parameter because the energy of the configuration depends only on the topological charge Q. This is a direct consequence of the scale-invariance of energy functional (39).

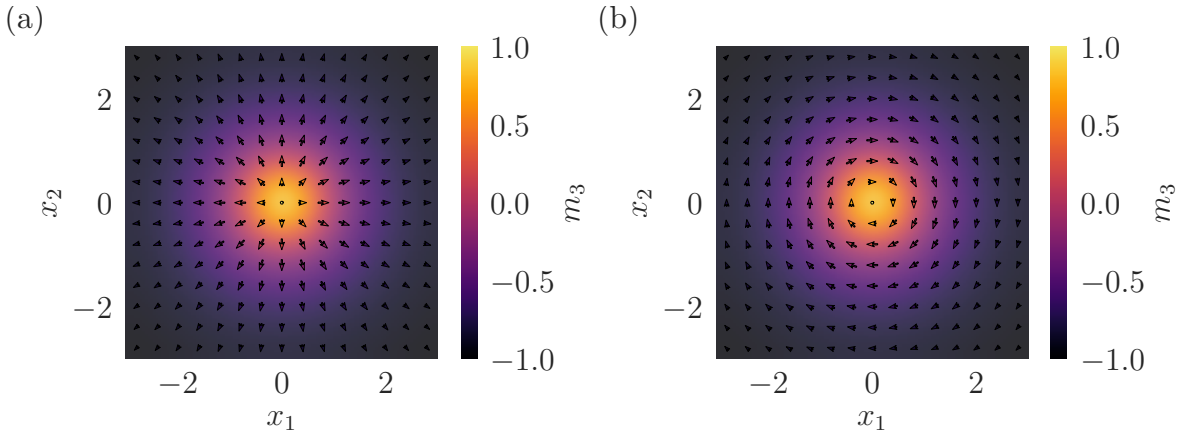

Figure 7. Projection of **m** on the plane for two isolated Belavin-Polyakov Skyrmions with different chirality. **(a)** $z_0 = 0$, $R_0 = 1$, $Q = 1$ and **(b)** $z_0 = 0$, $R_0 = e^{i\pi/2}$, $Q = 1$. The color map represents the x_3-axis component of the magnetization.

2.2. Skyrmions in chiral ferromagnets

Due to their meta-stable nature, Belavin-Polyakov skyrmions don't form in common FMs. However, Bogdanov and Yablonskii Bogdanov and Yablonskii (1989) predicted that Dzyaloshinskii-Moriya (DM) interactions, present in chiral magnets and asymmetric multilayers of magnetic materials CJiang et al. (2017a), could stabilize magnetic skyrmions. A prediction that was confirmed

by the experimental observation of a skyrmion lattice in the chiral ferromagnet MnSi Muhlbauer et al. (2009). Chiral FMs are commonly modeled with the energy functional

$$F[\mathbf{m}] = \int_{\mathbb{R}^3} \left[\mathscr{J}(\partial_\mu \mathbf{m})^2 + \mathscr{D}\mathbf{m} \cdot (\nabla_{-\alpha} \times \mathbf{m}) + \mathscr{K} m_3^2 - M_s B m_3 \right] d^3x, \tag{51}$$

where D is the DMI strength, K is the magnitude of a single-ion anisotropy (easy-axis for $K > 0$ and easy-plane for $K < 0$), M_s is the saturation magnetization, B is the magnitude of an external magnetic field applied in the x_3 direction and $\nabla_{-\alpha}$ is defined as

$$\nabla_{-\alpha} = \begin{pmatrix} \cos\alpha\partial_1 + \sin\alpha\partial_2 \\ -\sin\alpha\partial_1 + \cos\alpha\partial_2 \\ 0 \end{pmatrix}, \tag{52}$$

denoting a family of DMIs characterized by the parameter $\alpha \in [0, 2\pi)$.

2.2.1. Finding the optimal size. As opposed to Belavin-Polyakov skyrmions, we can expect skyrmion solutions that minimize (51) to have an optimal size because the addition of new interaction terms makes the energy functional no longer scale-invariant. To find the optimal size, we can use the Belavin-Polyakov solution (49) as a trial function and minimize energy functional (51) with respect to the free parameter R_0.

As introduced in Section 1.2, considering axisymmetric spin configurations $\theta(\rho)$ and $\alpha = 0$

brings energy functional (51) to the well-known form

$$F[\theta(\rho)] = 2\pi \int_0^\infty \left[\mathscr{J} \left(\left(\frac{d\theta}{d\rho} \right)^2 + \frac{\sin^2\theta}{\rho^2} \right) + \mathscr{D} \left(\frac{d\theta}{d\rho} + \frac{\sin(2\theta)}{2\rho} \right) + \mathscr{K} \sin^2\theta + M_s B(1-\cos\theta) \right] \rho d\rho. \tag{53}$$

Using a Belavin-Polyakov skyrmion with $Q = 1$, $z_0 = 0$ and $R_0 \in \mathbb{R}$ as our trial function, written in these coordinates as

$$\theta_{\mathrm{BP}}(\rho) = 2\arctan\left(\frac{R_0}{\rho}\right), \tag{54}$$

we can plug (54) into (53) and after integrating up to a radial distance R which we then make go to infinity, we get

$$\frac{F}{2\pi} = 4\mathscr{J} - 2\mathscr{D}R_0 - 2\mathscr{K}R_0^2 + (M_s B + 2\mathscr{K}) \lim_{R\to\infty} \ln\left(\frac{R^2+R_0^2}{R_0^2}\right), \tag{55}$$

which diverges unless $M_s B = -2\mathscr{K}$, requiring $\mathscr{K} < 0$. If this condition holds, the optimal skyrmion size (satisfying $\frac{dF}{dR_0} = 0$) is given by

$$R_0 = -\frac{\mathscr{D}}{2\mathscr{K}}. \tag{56}$$

Furthermore, it has been shown Döring and Melcher (2017) that a Belavin-Polyakov skyrmion with double this optimal size

$$\theta(\rho) = 2\arctan\left(-\frac{\mathscr{D}}{\mathscr{K}\rho}\right), \tag{57}$$

turns out to be an exact solution to the Euler-Lagrange equation associated with (26) and the relation $M_sB = -2\mathscr{K}$ is known as the solvable line.

We find then that the variational principle allowed us to find the condition under which our trial function is an exact solution to the Euler-Langrange equation of the system and gave us the correct solution (up to a factor of 2).

Condition $M_sB = -2K$ can be met in materials with an easy-plane anisotropy ($K < 0$), thus the solvable line should be accessible in real materials by fine-tuning the external magnetic field to

$$B_{\text{crit}} = \frac{2|K|}{M_s}. \tag{58}$$

2.2.2. Optimal size outside the solvable line. Outside the solvable line ($M_sB \neq -2\mathscr{K}$), Belavin-Polyakov skyrmions produce an infinite amount of energy and we are thus forced to change our trial function or resort to numerical analysis. In this section, we numerically explore the neighboring region to the solvable line by fine-tuning the external magnetic field to get to the solvable line and then changing it slightly.

Along the solvable line, energy functional (53) can be written in dimensionless variables as Barton-Singer et al. (2020)

$$\frac{F[\theta(\rho)]}{\mathscr{J}} = 2\pi \int_0^\infty \left[\left(\frac{d\theta}{d\rho}\right)^2 + \frac{\sin^2\theta}{\rho^2} + \left(\frac{d\theta}{d\rho} + \frac{\sin(2\theta)}{2\rho}\right) + k(1-\cos\theta)^2 \right] \rho d\rho,$$

where $k = \frac{\mathscr{J}|\mathscr{K}|}{\mathscr{D}^2}$.

To explore the behavior outside the solvable line we introduce an additional magnetic field term of magnitude $\Delta h = \frac{\mathscr{J} M_s \Delta B}{\mathscr{D}^2}$ where ΔB quantifies how far from the critical field $B_{\text{crit}} = \frac{2|\mathscr{K}|}{M_s}$ the magnetic field is. The resulting energy functional is

$$\frac{F[\theta(\rho)]}{2\pi\mathscr{J}} = \int_0^\infty \left[\left(\frac{d\theta}{d\rho}\right)^2 + \frac{\sin^2\theta}{\rho^2} + \left(\frac{d\theta}{d\rho} + \frac{\sin(2\theta)}{2\rho}\right) + k\sin^2\theta + \Delta h(1-\cos\theta) \right] \rho d\rho. \tag{59}$$

Assuming material parameters from thin films of $Fe_{0.7}Co_{0.3}Si$ Vousden et al. (2016)

$$\mathscr{J} = 4.0\times10^{-13}\,\frac{\mathrm{J}}{\mathrm{m}^1}, \quad \mathscr{D} = 2.7\times10^{-4}\,\frac{\mathrm{J}}{\mathrm{m}^2}, \quad \mathscr{K} = -3.0\times10^{4}\,\frac{\mathrm{J}}{\mathrm{m}^3}, \quad \mathrm{M_s} = 9.5\times10^{4}\,\frac{\mathrm{A}}{\mathrm{m}},$$

a magnetic field $B_{\text{crit}} = 0.631579\,\mathrm{T}$ is needed to bring this material to the solvable line. Outside the solvable line, we use a Monte-Carlo method (see Section 1.2.1 for details) to find minima of (59) subject to the boundary conditions

$$\theta(0) = \pi \qquad \text{and} \qquad \theta(\infty) = 0. \tag{60}$$

Skyrmion profiles for $\Delta h > 0$ are shown in Figure 8. Defining the size of a skyrmion as $\rho(\theta = \pi/2)$, Figure 8 shows how the skyrmion size changes with the additional magnetic field applied. We can see the skyrmion size decreases with increasing magnetic field and we can expect the size to asymptotically approach zero, since the Zeeman term in the energy functional favors a ferromagnetic phase with $m_3 = 1$.

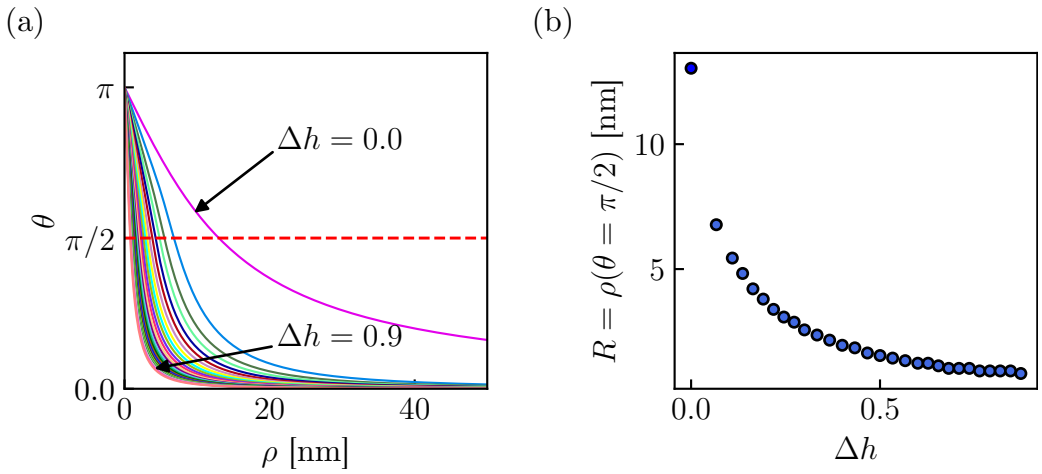

Figure 8. (a) Isolated skyrmion profiles outside the solvable line for $\Delta h > 0$. It is clear how the increase of the magnetic field narrows the skyrmion profile. (b) Dependence of the skyrmion size on Δh. The decrease in the skyrmion size is steep near the critical line and asymptotic as Δh gets closer to unity.

We can compare our numerical results with ansatze for the skyrmion profile that are commonly used in the literature. We will consider the 360° domain wall profile Braun (1994)

$$\theta_{\mathrm{DW}}(\rho) = 2\arctan\left[\frac{\sinh(R/w)}{\sinh(\rho/w)}\right], \tag{61}$$

where R is the radius of the domain wall and w is the wall width. As well as a modified Belavin-Polyakov profile

$$\theta_{\mathrm{MBP}}(\rho) = 2\arctan\left(\frac{R_0}{\rho}\right)e^{-\lambda\rho}, \tag{62}$$

where R_0 is the size of the skyrmion and λ was introduced as a cut-off to keep the energy of the profile finite.

Varying the parameters of each ansatz to minimize energy functional (59), in Figure 9 we

show how the optimal profiles compare to the numerical solution near and far from the solvable line. We find that, close to the solvable line, both ansatze reproduce the general behavior of the numerical solution. Far from the solvable line, both ansatze agree well with the numerical solution. This suggests that, at least for easy-axis chiral ferromagnets, the modified Belavin-Polyakov solution we proposed could be used effectively to study the properties of ferromagnetic skyrmions analytically.

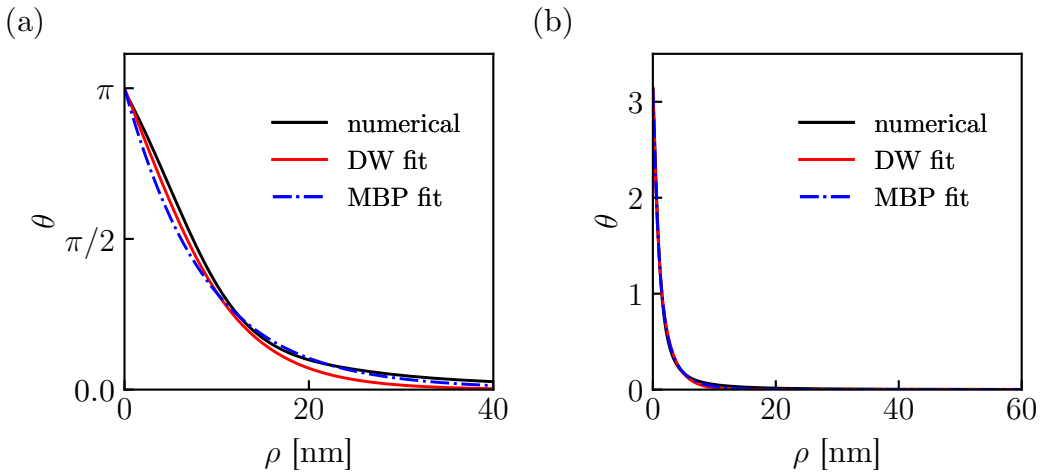

Figure 9. Comparison between optimal ansatzes and numerical solution. (a) Near the solvable line at $\Delta h = 0.06$ both ansatzes fail to capture the numerical solution exactly. (b) Far from the solvable line at $\Delta h = 0.8$ both ansatzes capture the general behavior very well.

The case $\Delta h < 0$ was not considered here because the preferred homogeneous state is a canted ferromagnetic phase Ross et al. (2021), which changes the form of the energy functional (59) as well as the boundary conditions (28).

2.3. Discussion

The continuous model of two-dimensional chiral ferromagnets has been used extensively in the past to study the properties of skyrmions in thin films Zhang et al. (2016); Leonov et al. (2016).

Recently, it has gained attention from theoretical studies that have successfully constructed exact skyrmion solutions for this model, assuming a specific choice of material parameters Schroers (2019); Walton (2020); Hill et al. (2021); Ross et al. (2021). In this chapter, we have studied this continuous model analytically and we have shown how a simple analysis of the scale of an isolated skyrmion solution hints at the existence of the exact theoretical solutions that have been recently studied. We started by highlighting the scale-invariant nature of the isotropic energy functional and therefore of its simplest skyrmion solution: the Belavin-Polyakov skyrmion. Considering a more complicated energy functional like the one for a chiral ferromagnet which is not scale-invariant, we expected the solution to no longer be scale-invariant. As such, we added the scale or size of a skyrmion as a variational parameter in the Belavin-Skyrmion solution and used it as a trial function to minimize the energy functional. This easily gave us a restriction in the material parameters under which the energy was kept finite and an estimate for the optimal size of the skyrmion. Interestingly, this was exactly the condition assumed in recent theoretical studies to construct new exact skyrmion solutions. To explore solutions outside this specific choice of material parameters we varied the magnetic field and studied its size using numerical solutions.

Finally, we proposed a new trial function for isolated skyrmions that fits the numerical solutions we obtained just as well as the widely used domain-wall profile.

3. Antiferromagnetic skyrmions

Until now we have only considered skyrmions in ferromagnetic materials. But as was outlined in Chapter , when driven by an electric current, ferromagnetic skyrmions experience the skyrmion Hall effect: a transverse deflection from the direction of the current. This makes them inadequate for the skyrmion-based racetrack memory. Skyrmions in antiferromagnetic materials on the other hand, due to the net compensation of topological charge, do not experience the skyrmion Hall effect, making them ideal for the skyrmion-based racetrack memory.

In this chapter, we explore the phase diagram of chiral antiferromagnets with a square lattice structure looking for stable skyrmionic structures. In Section 3.1, we simulate a chiral antiferromagnet at zero temperature using a continuum model and look for isolated skyrmions. We study the behavior of the skyrmion size and energy as a function of the material parameters, with the intent of finding possibly stable skyrmion phases. In Section 3.2, we simulate a square lattice chiral antiferromagnet at finite temperature using Monte Carlo simulations and explore a wide region of the phase space. We create a low-temperature phase diagram and study the effects of applying magnetic fields to the material.

3.1. Isolated skyrmions

In the same spirit as Chapter 2, we can use models of isolated antiferromagnetic skyrmions in an infinitely big material to study the general properties of antiferromagnetic skyrmions. We will model a chiral antiferromagnet with easy-axis anisotropy in the z-direction in the presence of

an external magnetic field also in the z-direction. The energy functional for such a system reads

$$F_{\mathrm{AF}}[\mathbf{m}] = \int_{\mathbb{R}^3} \left[\mathscr{J}\,(\partial_\mu \mathbf{m})^2 + \mathscr{D}\mathbf{m}\cdot(\nabla\times\mathbf{m}) - \mathscr{K} m_3^2 + \frac{(M_s B)^2}{32A}(m_3^2 - 1) \right] d^3x, \tag{63}$$

where D is the DMI strength, K is the magnitude of the anisotropy, M_s is the saturation magnetization and B is the magnitude of an external magnetic field.

Considering axis-symmetric configurations and introducing dimensionless variables (see Section 1.2 for details) this energy functional can be written as

$$\frac{F[\theta(r)]}{2\pi\mathscr{J}} = \int_0^\infty \left[\left(\left(\frac{d\theta}{dr}\right)^2 + \frac{\sin^2\theta}{r^2} \right) + \left(\frac{d\theta}{dr} + \frac{\sin(2\theta)}{2r} \right) + g\sin^2\theta \right] r dr, \tag{64}$$

where $g = \frac{\mathscr{J}}{\mathscr{D}^2}\left(\mathscr{K} - \frac{(M_s B)^2}{32\mathscr{J}}\right)$.

To explore the phase space of AFMs, we vary g to find the minima of energy functional (64) subject to boundary conditions (28). Once we obtain the lowest energy configuration, we record the energy and calculate its size. The resulting diagram Figure 10 contains a wide range of possible minima of (64). From this diagram, we can see that higher-sized skyrmions have energies lower than the saturated FM state, which suggests there is a region in the phase space of AFMs where skyrmions could be stable even in the absence of a magnetic field. Moreover, given that increasing the magnetic field B while keeping all other parameters fixed reduces the value of g we can conclude that a magnetic field increases the skyrmion size and decreases its energy, making it more stable. Nevertheless, a comparison with the energy of a helicoidal phase has to be made

before drawing any conclusions.

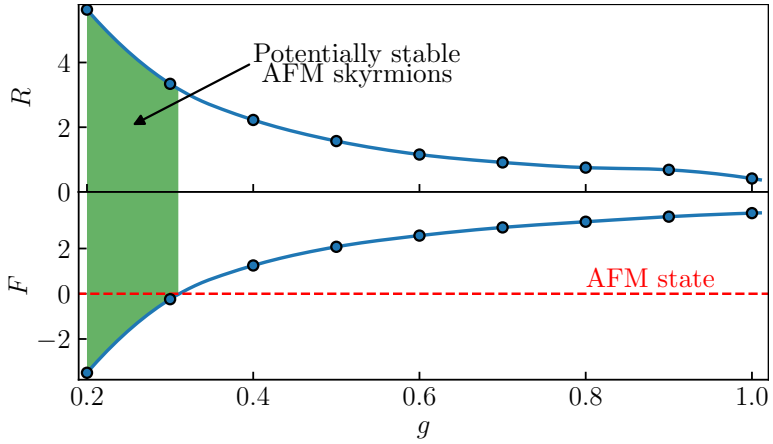

Figure 10. Size (R) and energy (F) behavior for different values of the free parameter g. We highlight in green a region where the skyrmion size is non-zero and the energy is lower than that of the antiferromagnetic state. In this region, isolated skyrmions could be the ground state of the system.

3.2. Discrete model

To determine if antiferromagnetic skyrmions can actually be the ground state of chiral antiferromagnets, we use Monte Carlo simulations to study the classical Heisenberg model of a chiral magnet introduced in Section 1.1. Assuming a homogeneous chiral antiferromagnet with easy-axis anisotropy and external magnetic field both along the z direction, the Hamiltonian takes the form

$$\mathscr{H} = \sum_{\langle i,j \rangle} \mathbf{S}_i \cdot \mathbf{S}_j - D \sum_{\langle i,j \rangle} \mathbf{e}_{ij} \cdot (\mathbf{S}_i \times \mathbf{S}_j) - K \sum_i (\mathrm{S}_i^z)^2 - B \sum_i \mathrm{S}_i^z, \tag{65}$$

where it was assumed that $J = 1$ and $\mathbf{e}_{ij}$ is the unit vector between the neighboring sites i and j. We simulated $120-160$ replicas of a square lattice consisting of $N = 20 \times 20 - 32 \times 32$ sites using parallel tempering Monte Carlo. A total amount of $8 - 12 \times 10^6$ MC sweeps were performed

where half of this amount was used for equilibration and the other half to calculate the averages of physical quantities. The exchange between replicas was carried out every 10 MC sweeps. Refer to Section 1.1 for a detailed explanation of the methods used.

The quantities we have calculated are the magnetization m, magnetic susceptibility χ_m, specific heat c and topological charge Q:

$$m = \frac{1}{N}\left\langle \sum_i \mathrm{S}_i^z \right\rangle, \tag{66}$$

$$\chi_m = \beta N \left\langle m^2 \right\rangle - \left\langle m \right\rangle^2, \tag{67}$$

$$c = \frac{\beta^2}{N}\left\langle E^2 \right\rangle - \left\langle E \right\rangle^2, \tag{68}$$

$$Q = \frac{1}{4\pi}\left\langle \left| \sum_i^N \left(A_i^{(12)} \mathrm{sign}[\chi_\mathrm{i}^{(12)}] + \mathrm{A}_\mathrm{i}^{(34)} \mathrm{sign}[\chi_\mathrm{i}^{(34)}] \right) \right| \right\rangle, \tag{69}$$

see Section 1.1.2 for more details on the definition of Q.

3.2.1. Zero-field behavior. Setting $B = 0$ in the Hamiltonian (65) we constructed the low-temperature $K - D$ phase diagram presented in Figure 11 along with the real space spin configurations and structure factors of each of these phases as shown in Figure 12.

At $D = K = 0$, we observe a canted antiferromagnetic phase (CAF) as can be seen in the central peaks on both magnetic structure factors. The existence of this phase is expected to be a finite-size effect due to Mermin-Wagner's theorem forbidding spontaneous symmetry breaking in the two-dimensional Heisenberg model. For higher anisotropy strengths and low Dzyaloshinskii–Moriya strengths, we find that the antiferromagnetic phase (AF) is the ground state character-

ized by a central peak in the out-of-plane structure factor. On the other hand, when the Dzyaloshinskii–Moriya strength is higher while the anisotropy strength is low, the periodic spiral phase (SP) prevails. This phase consists of two intertwined spirals on each sublattice described by a non-null wave vector identified by the two peaks in the structure factors.

In between the AF and SP phases, we found that AFM skyrmions can be stabilized in the form of a skyrmion gas (SKG), characterized in the structure factor by the blending of the six Bragg peaks of a skyrmion lattice phase into a broad circle shape Rosales et al. (2022).

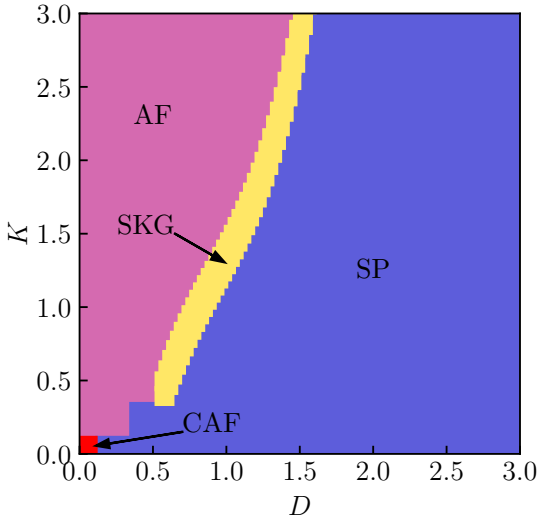

Figure 11. Zero field and low-temperature $K-D$ phase diagram of the spin model described by the Hamiltonian (65). We observe a skyrmion gas phase (SKG) appear between the spiral (SP) and anitferromagnetic phases. The different phases were identified using the topological charge, real space configurations and structure factors presented in Figure 12.

3.2.2. Magnetic field and temperature dependence. To understand the effects of the magnetic field, we start by examining the field dependence of the magnetic and topological order parameters m and Q. We fix $D = K = 0.7$ and $T = 0.01$ which places us inside the SKG phase and simulate the system for increasing values of B. The results are shown in Figure 13. We observe

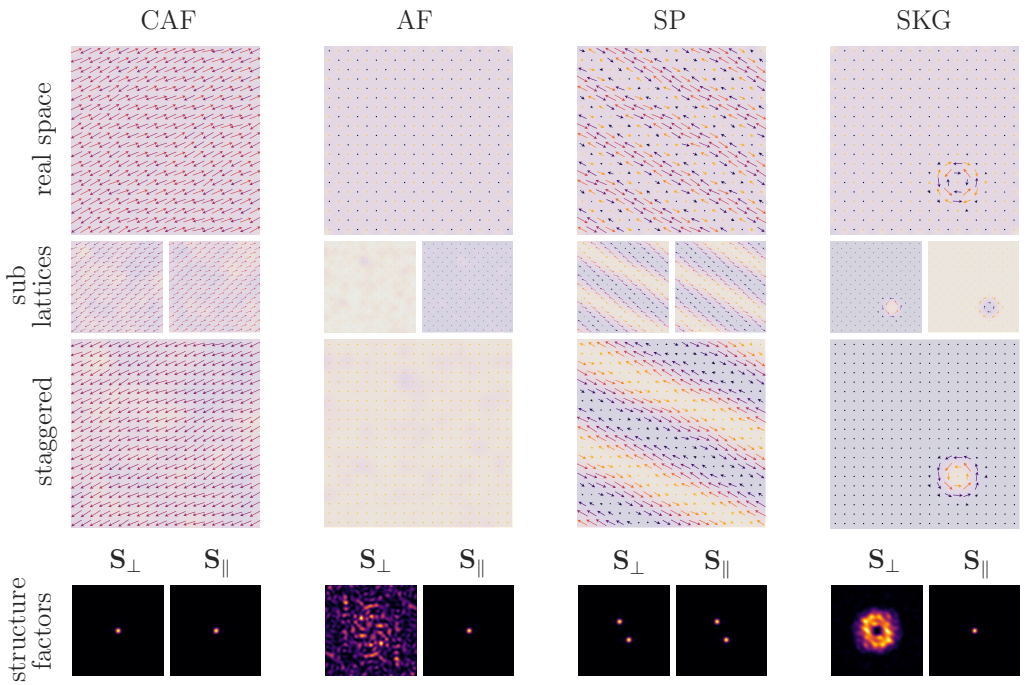

Figure 12. Low-temperature phases obtained in the MC simulations of the spin model described by the Hamiltonian (65) at $B = 0$. The staggered spin configuration was obtained by inverting the spins in one of the sublattices as illustrated in Figure 6.

the magnetization increase monotonically with the magnetic field and three discontinuous jumps can be seen. The first discontinuity at $B \approx 0.97$ coincides with a discontinuous decrease to zero on the topological charge, upon inspection of the spin configurations and the structure factors this jump indicates a phase transition from the SKG phase to the SP phase. The second discontinuity at $B \approx 2.18$ is a transition from the SP phase to another SP phase with a wave vector of a bigger magnitude. The last discontinuity at $B = 3.75$ constitutes the transition from the SP phase to a field-polarized (FP) phase.

The evolution of the different phases with increasing temperature can be tracked from the behavior of the specific heat c and the magnetic susceptibility χ_m. In Figure 14 we present the

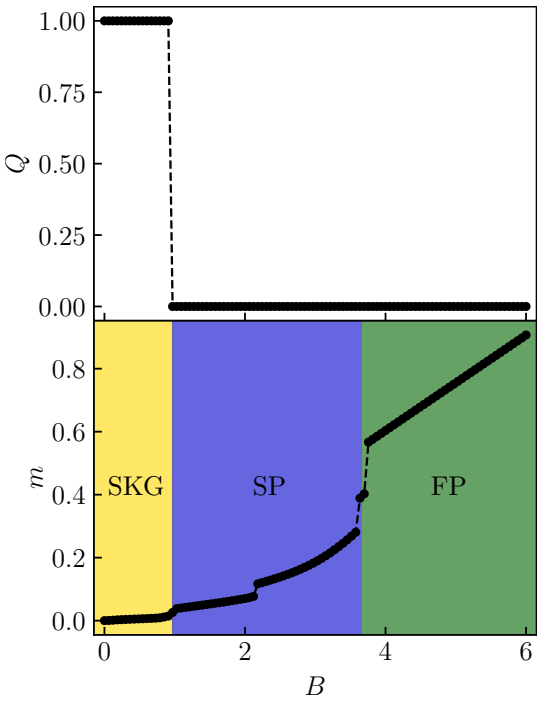

Figure 13. Field dependence of the magnetization m and topological charge Q at $D = K = 0.7$ and $T = 0.01$. The discontinuity in Q at $B \approx 0.97$ coincides with a jump in m and indicates the transition from the SKG phase to the SP phase. The jump in m at $B \approx 2.18$ corresponds to a transitions between to spiral phases. Finally at $B = 3.75$ we see a jump in m that indicates the start of a field-polarized phase.

temperature dependence of the specific heat at zero field. We observe two peaks that define the transition temperatures for phase transitions from the SKG phase to the SP phase and from the SP phase to a paramagnetic phase (PARA). For non-zero magnetic fields, the magnetic susceptibility is also expected to show peaks at transition temperatures. This can be seen in Figure 15, where we can see the field dependence of the transition temperatures.

In Figure 16 we present the full $B-T$ diagram for the system at $D = K = 0.7$. The diagram was constructed supplementing the information of Figures 13, 14 and 15, with the inspection of the spin configurations and the structure factors as displayed in Figure 17. We can see that the

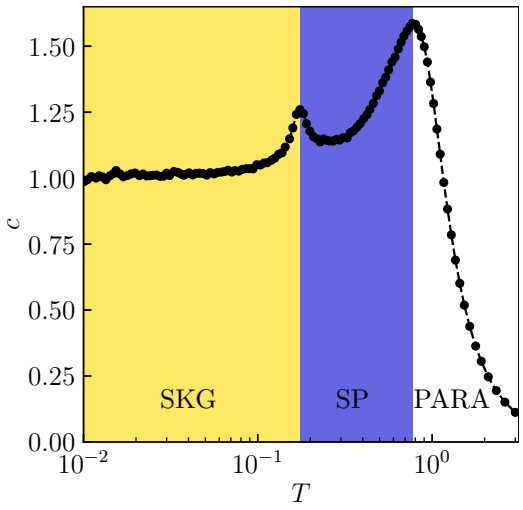

Figure 14. Temperature dependence of the specific heat c at zero magnetic field at $D = K = 0.7$. The peak in c at $T \approx 0.17$ corresponds to the transition from the SKG phase to the SP phase. The peak at $T \approx 0.78$ indicates the transition to the PARA phase.

SKG phase is stable up to magnetic fields of $B \approx 0.97$ and temperatures of about $T \approx 0.17$. Below $T \approx 0.17$, increasing the magnetic field beyond $B \approx 0.97$ induces a transition to an SP phase. This agrees with the effect the magnetic field has on an AFM in the continuum limit, namely, that its presence renormalizes the anisotropy as

$$K \to K - \frac{(M_s B)^2}{32A}. \tag{70}$$

Hence breaking the careful balance between the anisotropy and DMI strengths we observed in Figure 11. A further increase in the magnetic field past $B = 3.75$ makes the spins flop into a partially field-polarized phase (FP). This phase presents ferromagnetic order in the z direction and antiferromagnetic order in the $x - y$ plane. It is expected that at higher fields a fully ferromagnetic phase prevails.

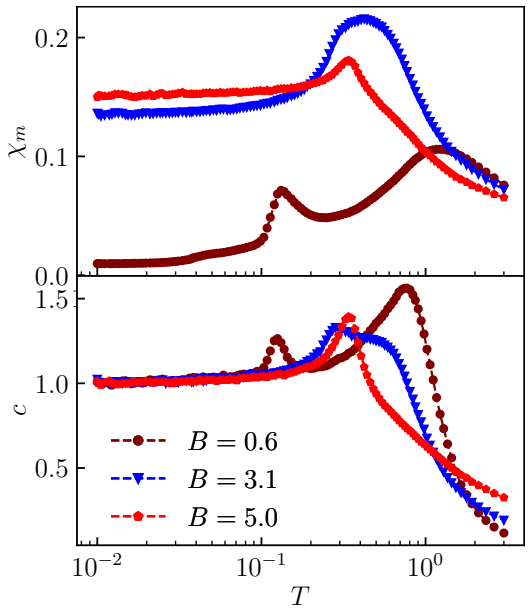

Figure 15. Temperature dependence of the specific heat c and the magnetic susceptibility χ_m for different values of the magnetic field at $D = K = 0.7$. We observe the magnetic field changes the thermally activated phase transitions considerably.

The effect of the magnetic field on the shape of the skyrmion itself can be examined by looking at the real-space spin configuration. In Figure 18 we see how the skyrmion diameter increases with increasing magnetic fields.

Finally, for our specific choice of parameters, the temperature interval where the SKG phase is stabilized goes up to $T = 0.17J$. Beyond this value, the spiral phase prevails independently of the magnetic field.

3.3. Discussion

In this chapter, we have studied continuous and discrete models of chiral antiferromagnets with easy-axis anisotropy looking for stable skyrmion phases. In the continuous picture, we focused on the properties of isolated skyrmions. Since the work by Bogdanov Bogdanov et al. (2002)

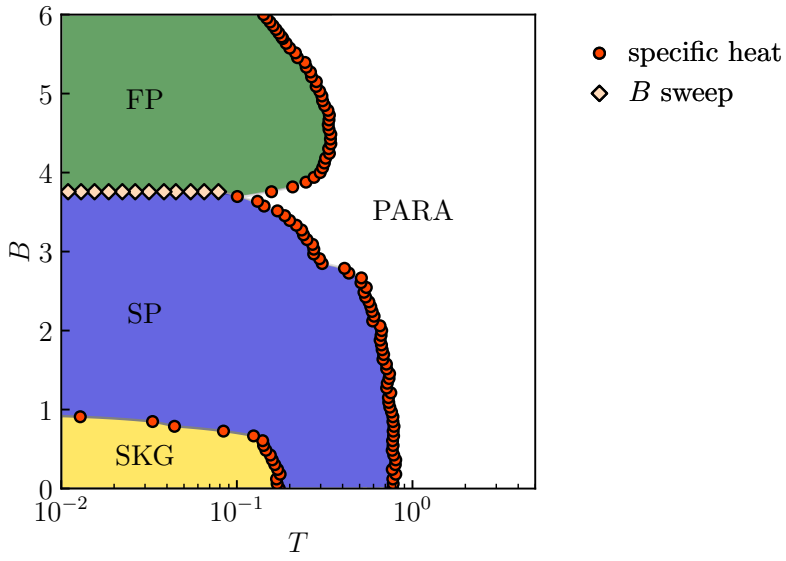

Figure 16. $B-T$ diagram at $D = K = 0.7$. The red circles denote the transition line obtained from the peaks of specific heat and the green rhombuses denote the transition line obtained by an inspection of the spin configuration and the structure factor.

it has been predicted that isolated skyrmions are possible configurations in these systems. Furthermore, the stability of isolated skyrmions has been studied using discrete models Bessarab et al. (2019b); Potkina et al. (2020). In these studies, it was established that contrary to ferromagnetic skyrmions, the stability of isolated antiferromagnetic skyrmions (quantified by the activation energy and the skyrmion size) was enhanced in the presence of a magnetic field. In Section 3.1, we intended to reproduce these results using a purely continuous description of isolated antiferromagnetic skyrmions. We found that in the continuum limit, with the right choice of units, there is a single dimensionless free parameter

$$g = \frac{A}{D^2}\left(K - \frac{(M_s B)^2}{32A}\right), \tag{71}$$

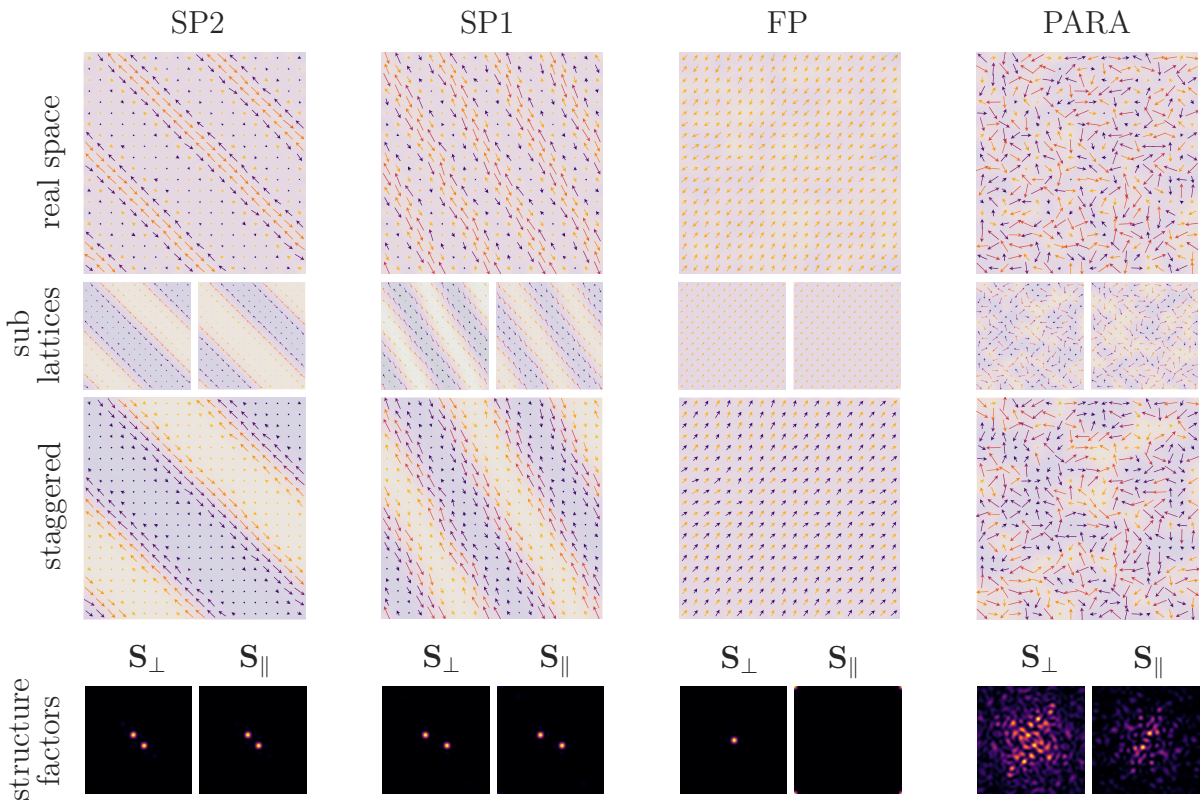

Figure 17. Phases induced by the magnetic field and temperature in the MC simulations of the spin model described by the Hamiltonian (65) at $D = K = 0.7$. The two spiral phases differ only by the absolute magnitude of the reciprocal vector describing each spiral and they were not differentiated in phase diagram 16.

that characterizes the isolated skyrmion. Studying the skyrmion size and energy as a function of this parameter yielded an interval where the isolated skyrmions have a finite size and lower energy than the saturated antiferromagnetic phase. Moreover, from the magnetic field dependence of parameter g, we can see that increasing the magnetic field while keeping the material parameters fixed results in a decrease in g. This, according to our results, corresponds to an increase in the skyrmion size as well as a decrease in the energy of the skyrmion. These facts indicate that the isolated skyrmion is more stable in the presence of a magnetic field, in accordance with the results

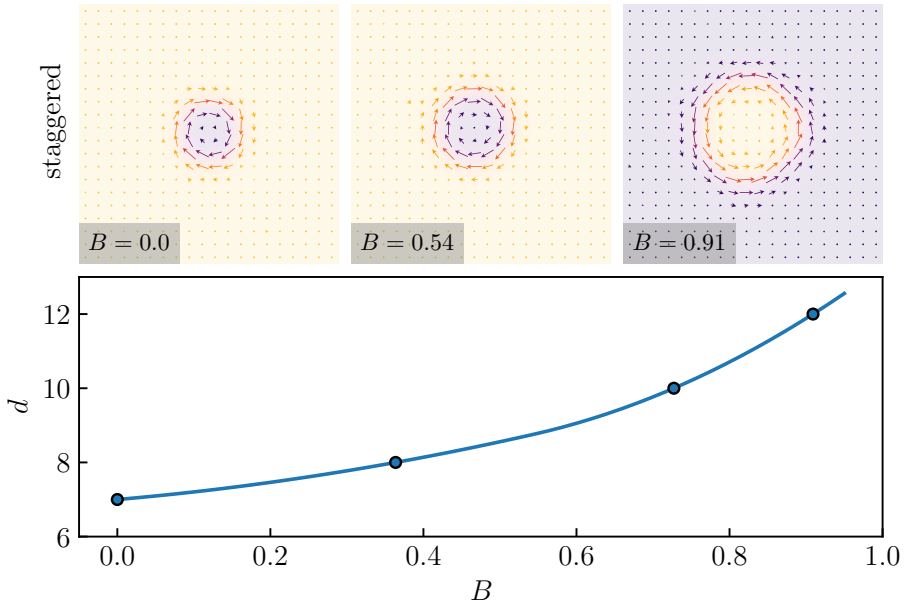

Figure 18. Magnetic field dependence of the skyrmion diameter d, depicting how skyrmions get bigger at higher magnetic fields. The staggered spin configuration is presented for clarity.

obtained by the studies that were previously mentioned.

Given that our simulations of isolated antiferromagnetic skyrmions suggest that they can be stable in a region of phase space, we wanted to verify whether or not antiferromagnetic skyrmion phases were stabilized in discrete squared lattice systems. Discrete models of our system have been explored at low temperatures by Zhang et al. Zhang et al. (2016), Keesman et al. Keesman et al. (2016) and Bessarab et al Bessarab et al. (2019b). Zhang et al. found using micromagnetics simulations that isolated antiferromagnetic skyrmions could be created without magnetic fields in small nanodisks and nanotracks using spin-polarized currents. Keesman et al. found using Monte Carlo simulations that antiferromagnetic skyrmion lattices did not form but in a finite-sized system with open boundaries, isolated skyrmions could form. Finally, Besserab et al. showed using relaxation methods that isolated skyrmions could form in a system with periodic boundary conditions

and, as was mentioned before, that their stability was increased by the presence of a magnetic field. In Section 3.2 we used parallel tempering Monte Carlo simulations to explore the phase diagram of small discrete systems (made out of 400 to 1024 spins) with periodic boundary conditions. The parallel tempering algorithm allowed us to study the temperature dependence of the phase diagram which was not explored in the previous studies. We constructed a low temperature and no field phase diagram that agrees qualitatively with the results obtained by Zhang et al., namely, that an antiferromagnetic skyrmion phase could be formed between a fully antiferromagnetic phase and a spiral/worm domain phase. According to our simulations, this phase corresponds to a skyrmions gas phase that forms at higher anisotropies strengths than those considered in the work by Keesman et al. Furthermore, placing ourselves inside the skyrmion gas phase, we considered the effect of magnetic fields and created a $B-T$ diagram. We found that, in agreement with the previous works and the continuum model, the magnetic field increases the size of the skyrmions in the skyrmion gas phase. We observed however that beyond a temperature-dependent critical field, the ground state shifted to a spiral phase. In addition to this we found that, for a specific choice of parameters, this skyrmion phase was stable up to $k_BT = 0.17J$. In studies of triangular lattice systems with similar Hamiltonians Rosales et al. (2015); Mohylna et al. (2021), antiferromagnetic skyrmion lattice phases are shown to be stable up to $k_BT = 0.3-0.4J$. This makes the thermal stability of the skyrmion gas phase we simulated comparatively lower. An extension of this work is to study the dependence of the higher possible temperature at which the skyrmion phase is stable on the material parameters and whether or not this temperature can increase.

4. Conclusion

Research on magnetic skyrmions has been a hot topic over the last decade due to their intrinsic theoretical richness as well as their promising features as information carriers. But despite all the interest in the field, there remain big open problems. From a purely theoretical perspective, even the simplest models of chiral magnetic skyrmions have a strong nonlinear character and obtaining analytical solutions is a difficult problem. From a technological perspective, it has been found that moving skyrmions along a magnetic track is not as easy a problem as once thought. In this thesis, we discussed and expand on recent developments that have accomplished progress on each of these fronts: solvable models of easy-plane chiral magnets and antiferromagnetic skyrmions respectively.

For the theoretically oriented part of this thesis, we began by reproducing the classic work on magnetic skyrmions by Belavin and Polyakov. We next showed how a variational analysis of the optimal scale of an isolated skyrmion can easily hint at the existence of a special kind solvable of models (solvable line) of easy-plane chiral ferromagnets that have recently been studied. Furthermore, with the intent of bridging the gap between these theoretical results and actual experiments, we used numerical methods to calculate isolated skyrmion solutions for a real easy-plane chiral ferromagnet: $Fe_{0.7}Co_{0.3}Si$. We found that the size of isolated skyrmions outside the solvable line decreases quickly for this material. Finally, we proposed a trial function for the skyrmion profile that accurately describes the behavior of these isolated skyrmions.

With adaptations to the numerical methods we developed for this part of the thesis, we

expect to be able to construct isolated skyrmion solutions on regions of the phase space of easy-plane chiral ferromagnets where the preferred homogeneous phase is not a fully antiferromagnetic phase but a canted ferromagnetic phase.

On the technologically oriented part, we simulated chiral antiferromagnets focusing on finding possibly stable antiferromagnetic skyrmion phases. We started by finding isolated antiferromagnetic skyrmion solutions to the continuum model of a chiral antiferromagnet. We established there is a region of phase space where isolated skyrmions are potentially stable and found that a magnetic field increases the stability of isolated antiferromagnetic skyrmions. With this promising result in mind, we used parallel tempering Monte Carlo simulations to construct the phase diagram of a square lattice chiral antiferromagnet. We found that there is a small region of phase space where the ground state of the system is a skyrmion gas phase. Moreover, we confirmed that a magnetic field increases the size of the antiferromagnetic skyrmions up to a critical field that depends on the temperature. Additionally, we observed that the temperature interval where this phase remained stable is lower compared to the antiferromagnetic skyrmions found in the triangle lattice. The results of this part of the thesis are in agreement with two previously established facts about antiferromagnetic skyrmions in the square lattice: that a lattice of antiferromagnetic skyrmions cannot form in a material with periodic boundary conditions and that magnetic fields increase the stability of antiferromagnetic skyrmions. Moreover, our results constitute an expansion of the existing knowledge of the thermal and magnetic field stability of antiferromagnetic skyrmions.

As future work, it is interesting to study the dependence of the temperature window where the skyrmion gas phase is stable on the material parameters. Additionally, with little adaptation

of the Monte Carlo methods we used, more complicated bipartite lattices can be simulated and a carbon copy of this study could be made.

Bibliography

Barton-Singer, B., Ross, C., and Schroers, B. J. (2020). Magnetic Skyrmions at Critical Coupling. *Communications in Mathematical Physics*, 375(3):2259–2280.

Belavin, A. A. and Polyakov, A. M. (1975). Metastable states of two-dimensional isotropic ferromagnets. *JETP Letters*, 22(10):245.

Berg, B. and Lüscher, M. (1981). Definition and statistical distributions of a topological number in the lattice O(3) σ-model. *Nuclear Physics B*, 190(2):412–424.

Berg, B. A. (2004). *Markov Chain Monte Carlo Simulations and Their Statistical Analysis*. WORLD SCIENTIFIC.

Bessarab, P. F., Yudin, D., Gulevich, D. R., Wadley, P., Titov, M., and Tretiakov, O. A. (2019a). Stability and lifetime of antiferromagnetic skyrmions. *Physical Review B*, 99(14):1–6.

Bessarab, P. F., Yudin, D., Gulevich, D. R., Wadley, P., Titov, M., and Tretiakov, O. A. (2019b). Stability and lifetime of antiferromagnetic skyrmions. *Physical Review B*, 99(14):1–6.

Bogdanov, A. (1995). New localized solutions of the nonlinear field equations. *JETP Letters*, 62(3):247.

Bogdanov, A. and Hubert, A. (1994). Thermodynamically stable magnetic vortex states in magnetic crystals. *Journal of Magnetism and Magnetic Materials*, 138(3):255–269.

Bogdanov, A. and Hubert, A. (1999). Stability of vortex-like structures in uniaxial ferromagnets. *Journal of Magnetism and Magnetic Materials*, 195(1):182–192.

Bogdanov, A. N. and Rößler, U. B. (2001). Chiral symmetry breaking in magnetic thin films and multilayers. *Physical Review Letters*, 87(3):37203–1–37203–4.

Bogdanov, A. N., Rößler, U. K., Wolf, M., and Müller, K. H. (2002). Magnetic structures and reorientation transitions in noncentrosymmetric uniaxial antiferromagnets. *Physical Review B - Condensed Matter and Materials Physics*, 66(21):1–16.

Bogdanov, A. N. and Yablonskii, D. A. (1989). Thermodynamically stable vortices in magnetically ordered crystals. *Sov Phys JETP*, 68(16):101.

Böttcher, M., Heinze, S., Egorov, S., Sinova, J., and Dupé, B. (2018). B-T phase diagram of Pd/Fe/Ir(111) computed with parallel tempering Monte Carlo. *New Journal of Physics*, 20(10).

Braun, H. B. (1994). Fluctuations and instabilities of ferromagnetic domain-wall pairs in an external magnetic field. *Phys. Rev. B*, 50(22):16485.

Buessen, F. (2021). Spinmc.jl: Classical monte carlo simulations for lattice spin systems. `https://github.com/fbuessen/SpinMC.jl`.

Döring, L. and Melcher, C. (2017). Compactness results for static and dynamic chiral skyrmions near the conformal limit. *Calculus of Variations and Partial Differential Equations*, 56(3):1–30.

Dzyaloshinsky, I. (1958). A thermodynamic theory of "weak" ferromagnetism of antiferromagnetics. *Journal of Physics and Chemistry of Solids*, 4(4):241–255.

Everschor-Sitte, K., Masell, J., Reeve, R. M., and Kläui, M. (2018). Perspective: Magnetic skyrmions - Overview of recent progress in an active research field. *Journal of Applied Physics*, 124(24).

Göbel, B. (2020). *Emergent electrodynamics in non-collinear spin textures (Ph.D. thesis)*. PhD thesis, Martin-Luther-Universität Halle-Wittenberg.

Göbel, B., Mertig, I., and Tretiakov, O. A. (2021). Beyond skyrmions: Review and perspectives of alternative magnetic quasiparticles. *Physics Reports*, 895:1–28.

Göbel, B., Mook, A., Henk, J., and Mertig, I. (2017). Antiferromagnetic skyrmion crystals: Generation, topological Hall, and topological spin Hall effect. *Physical Review B*, 96(6):1–5.

Gómez Albarracín, F. A. and Rosales, H. D. (2022). Machine learning techniques to construct detailed phase diagrams for skyrmion systems. *Physical Review B*, 105(21):214423.

Hill, D., Slastikov, V., and Tchernyshyov, O. (2021). Chiral magnetism: A geometric perspective. *SciPost Physics*, 10(3):1–23.

Hukushima, K. and Nemoto, K. (1996). Exchange Monte Carlo Method and Application to Spin Glass Simulations. *Journal of the Physical Society of Japan*, 65(6):1604–1608.

Jiang, W., Chen, G., Liu, K., Zang, J., te Velthuis, S. G., and Hoffmann, A. (2017a). Skyrmions in magnetic multilayers. *Physics Reports*, 704:1–49.

Jiang, W., Zhang, X., Yu, G., Zhang, W., Wang, X., Benjamin Jungfleisch, M., Pearson, J. E., Cheng, X., Heinonen, O., Wang, K. L., Zhou, Y., Hoffmann, A., and Te Velthuis, S. G. (2017b). Direct observation of the skyrmion Hall effect. *Nature Physics*, 13(2):162–169.

Joyce, G. S. (1967). Classical Heisenberg model. *Physical Review*, 155(2):478–491.

Keesman, R., Raaijmakers, M., Baerends, A. E., Barkema, G. T., and Duine, R. A. (2016). Skyrmions in square-lattice antiferromagnets. *Physical Review B*, 94(5):1–7.

Kezsmarki, I., Bordacs, S., Milde, P., Neuber, E., Eng, L. M., White, J. S., Rønnow, H. M., Dewhurst, C. D., Mochizuki, M., Yanai, K., Nakamura, H., Ehlers, D., Tsurkan, V., and Loidl, A. (2015). Neel-type skyrmion lattice with confined orientation in the polar magnetic semiconductor GaV4S8. *Nature Materials*, 14(11):1116–1122.

Kroese, D. P., Taimre, T., and Botev, Z. I. (2011). *Handbook of Monte Carlo Methods*. Wiley Series in Probability and Statistics. Wiley.

Leonov, A. O., Monchesky, T. L., Romming, N., Kubetzka, A., Bogdanov, A. N., and Wiesendanger, R. (2016). The properties of isolated chiral skyrmions in thin magnetic films. *New Journal of Physics*, 18(6).

Lévy, L. P. (2000). *Magnetism and Superconductivity*. Springer Berlin Heidelberg, Berlin, Heidelberg.

Manton, N. and Sutcliffe, P. (2004). *Topological Solitons*. Cambridge University Press, Cambridge.

Mohylna, M., Buša, J., and Žukovič, M. (2021). Formation and growth of skyrmion crystal phase in a frustrated Heisenberg antiferromagnet with Dzyaloshinskii-Moriya interaction. *Journal of Magnetism and Magnetic Materials*, 527.

Moriya, T. (1960). Anisotropic superexchange interaction and weak ferromagnetism. *Physical Review*, 120(1):91–98.

Muhlbauer, S., Binz, B., Jonietz, F., Pfleiderer, C., Rosch, A., Neubauer, A., Georgii, R., and Boni, P. (2009). Skyrmion Lattice in a Chiral Magnet. *Science*, 323(5916):915–919.

Nagaosa, N. and Tokura, Y. (2013). Topological properties and dynamics of magnetic skyrmions. *Nature Nanotechnology*, 8(12):899–911.

Newman, M. E. J. and Barkema, G. T. (1999). *Monte Carlo methods in statistical physics*. Clarendon Press.

Polyakov, A. M. (1987). *Gauge Fields and Strings*. Routledge.

Potkina, M. N., Lobanov, I. S., Jónsson, H., and Uzdin, V. M. (2020). Skyrmions in antiferromagnets: Thermal stability and the effect of external field and impurities. *Journal of Applied Physics*, 127(21).

Rosales, H. D., Cabra, D. C., and Pujol, P. (2015). Three-sublattice skyrmion crystal in the anti-

ferromagnetic triangular lattice. *Physical Review B - Condensed Matter and Materials Physics*, 92(21):1–8.

Rosales, H. D., Gómez Albarracín, F. A., Pujol, P., and Jaubert, L. D. C. (2022). A skyrmion fluid and bimeron glass emerging from competition with a chiral spin liquid. *arXiv e-prints*, page arXiv:2202.06993.

Ross, C., Sakai, N., and Nitta, M. (2021). Skyrmion interactions and lattices in chiral magnets: analytical results. *Journal of High Energy Physics*, 2021(2).

Rößler, U. K., Bogdanov, A. N., and Pfleiderer, C. (2006). Spontaneous skyrmion ground states in magnetic metals. *Nature*, 442(7104):797–801.

Schroers, B. J. (2019). Gauged sigma models and magnetic Skyrmions. *SciPost Physics*, 7(3):1–19.

Vousden, M., Albert, M., Beg, M., Bisotti, M. A., Carey, R., Chernyshenko, D., Cortés-Ortuño, D., Wang, W., Hovorka, O., Marrows, C. H., and Fangohr, H. (2016). Skyrmions in thin films with easy-plane magnetocrystalline anisotropy. *Applied Physics Letters*, 108(13).

Walton, E. (2020). On the geometry of magnetic Skyrmions on thin films. *Journal of Geometry and Physics*, 156.

Wang, X. S., Yuan, H. Y., and Wang, X. R. (2018). A theory on skyrmion size. *Communications Physics*, 1(1):1–7.

Yu, X. Z., Onose, Y., Kanazawa, N., Park, J. H., Han, J. H., Matsui, Y., Nagaosa, N., and Tokura, Y. (2010). Real-space observation of a two-dimensional skyrmion crystal. *Nature*, 465(7300):901–904.

Zhang, X., Zhou, Y., and Ezawa, M. (2016). Antiferromagnetic Skyrmion: Stability, Creation and Manipulation. *Scientific Reports*, 6:1–8.

Zhou, Y. (2019). Magnetic skyrmions: Intriguing physics and new spintronic device concepts. *National Science Review*, 6(2):210–212.

Apéndice A. Fundamentos de sólidos rígidos

The discrete Hamiltonian we study in the thesis reads

$$\mathscr{H} = -J \sum_{<i,j>} \mathbf{S}_i \cdot \mathbf{S}_j - D \sum_{<i,j>} \mathbf{e}_{ij} \cdot (\mathbf{S}_i \times \mathbf{S}_j) - K \sum_i (\mathrm{S}_i^z)^2 - B \sum_i \mathrm{S}_i^z. \tag{72}$$

To obtain the continuum limit of this Hamiltonian we approximate the spin configuration by the continuous magnetization $\mathbf{m}(\mathbf{r})$ which takes the values $\{\mathbf{S}_i\}$ on their respective positions $\{\mathbf{r}_i\}$. The Hamiltonian becomes then an energy functional of $\mathbf{m}(\mathbf{r})$.

The form of the on-site interactions does not change significantly with this approximation:

$$K \sum_i (\mathrm{S}_i^z)^2 \approx \mathscr{K} \int m_3^2 \, d^3x \quad ; \quad B \sum_i \mathrm{S}_i^z \approx M_s B \int m_3 \, d^3x, \tag{73}$$

where $\mathscr{K} = \frac{K}{a^3}$ and $\mathscr{B} = \frac{B}{a^3}$.

For the spin exchange interactions, we have to find a relationship between the value of the magnetization field of two neighboring sites. We do this by expanding the magnetization on a given site j, which neighbors site i, as:

$$\mathbf{m}(\mathbf{r}_j) = \mathbf{m}(\mathbf{r}_i \pm a\,\mathbf{e}_\alpha) = \mathbf{m}(\mathbf{r}_i) \pm a\,\partial_\alpha \mathbf{m}(\mathbf{r}_i), \tag{74}$$

where a is the lattice spacing. Now considering all the nearest-neighbor interactions and using expansion 74 the continuum form can easily be obtained. For the Heisenberg exchange interaction,

we obtain

$$
\begin{aligned}
-J\sum_{<i,j>}\mathbf{S}_i\cdot\mathbf{S}_j &= -\frac{J}{2}\sum_{<i,j>}\left[(\mathbf{S}_i^2+\mathbf{S}_j^2)^2-(\mathbf{S}_i-\mathbf{S}_j)^2\right]\\
&= \frac{J}{2}\sum_{<i,j>}(\mathbf{S}_i-\mathbf{S}_j)^2+\text{cte}\\
&= \frac{J}{2}\sum_{<i,j>}\left[\mathbf{m}(\mathbf{r}_i)-\mathbf{m}(\mathbf{r}_j)\right]^2+\text{cte}\\
&= \frac{J}{4}\sum_i\Big\{[\mathbf{m}(\mathbf{r}_i)-\mathbf{m}(\mathbf{r}_i+a\,\mathbf{e}_x)]^2+[\mathbf{m}(\mathbf{r}_i)-\mathbf{m}(\mathbf{r}_i-a\,\mathbf{e}_x)]^2+\\
&\qquad [\mathbf{m}(\mathbf{r}_i)-\mathbf{m}(\mathbf{r}_i+a\,\mathbf{e}_y)]^2+[\mathbf{m}(\mathbf{r}_i)-\mathbf{m}(\mathbf{r}_i-a\,\mathbf{e}_y)]^2\Big\}+\text{cte}\\
&= a^2\frac{J}{2}\sum_i\Big\{[\partial_x\mathbf{m}(\mathbf{r}_i)]^2+[\partial_x\mathbf{m}(\mathbf{r}_i)]^2\Big\}+\text{cte}\\
&\approx \mathscr{J}\int\left[\partial_\mu\mathbf{m}(\mathbf{r})\right]^2d^3x
\end{aligned}
$$

where $\mathscr{J}=\frac{J}{2a}$. And for the Dzyaloshinskii-Moriya interaction

$$
\begin{aligned}
-D\sum_{<i,j>}\mathbf{e}_{ij}\cdot(\mathbf{S}_i\times\mathbf{S}_j) &= -\frac{D}{2}\sum_i[\mathbf{e}_x\cdot(\mathbf{m}(\mathbf{r}_i)\times\mathbf{m}(\mathbf{r}_i+a\mathbf{e}_x))-\\
&\qquad \mathbf{e}_x\cdot(\mathbf{m}(\mathbf{r}_i)\times\mathbf{m}(\mathbf{r}_i-a\mathbf{e}_x))+\mathbf{e}_y\cdot(\mathbf{m}(\mathbf{r}_i)\times\mathbf{m}(\mathbf{r}_i+a\mathbf{e}_y))-\\
&\qquad\qquad \mathbf{e}_y\cdot(\mathbf{m}(\mathbf{r}_i)\times\mathbf{m}(\mathbf{r}_i-a\mathbf{e}_y))]\\
&= -D\sum_i[\mathbf{e}_x\cdot(\mathbf{m}(\mathbf{r}_i)\times a\,\partial_x\mathbf{m}(\mathbf{r}_i)+\\
&\qquad\qquad \mathbf{e}_y\cdot(\mathbf{m}(\mathbf{r}_i)\times a\,\partial_y\mathbf{m}(\mathbf{r}_i)]\\
&= aD\sum_i[m_x\partial_y m_z-m_y\partial_x m_z+m_z(\partial_x m_y-\partial_y m_x)]
\end{aligned}
$$

$$\approx \frac{D}{a^2}\int [m_x\partial_y m_z - m_y\partial_x m_z + m_z(\partial_x m_y - \partial_y m_x)]d^3x$$
$$\approx \mathscr{D}\int \mathbf{m}\cdot(\nabla\times\mathbf{m})\,d^3x$$

with $\mathscr{D} = \frac{D}{a^2}$.